METAL OXIDE NANOSTRUCTURES FOR ENERGY CONVERSION AND STORAGE

A Thesis

by

XING SUN

Submitted to the Graduate School of
The University of Texas-Pan American
In partial fulfillment of the requirements for the degree of

MASTER OF SCIENCE

May 2014

Major Subject: Chemistry

METAL OXIDE NANOSTRUCTURES FOR ENERGY CONVERSION AND STORAGE

A Thesis
by
XING SUN

COMMITTEE MEMBERS

Dr. Yuanbing Mao
Chair of Committee

Dr. Jason Parsons
Committee Member

Dr. Jose J. Gutierrez
Committee Member

Dr. John R. Villarreal
Committee Member

May 2014

Copyright 2014 Xing Sun
All Rights Reserved

ABSTRACT

Xing Sun, Metal Oxide Nanostructures for Energy Conversion and Storage. Master of Science (MS), May, 2014, 81 pp., 5 tables, 28 figures, references, 84 titles.

With the depletion of non-renewable resources and the related problems such as environmental pollutions and global warming effect, the society urgently needs more efficient and controllable energy conversion and storage systems. Three-dimensional ZnO nanoforests were prepared and morphology-tunable, which benefits both of energy conversion and storage systems. Willow-like ZnO nanoforests led the highest conversion efficiency of photoelectrochemical water splitting in reported pure ZnO nanostructures. Compared with nanowire arrays, ZnO@MnO_2 nanoforests delivered 5 times higher specific capacitances within the same footprint area. V_2O_5@PPy exhibited higher specific capacitance and better rate stability than pure V_2O_5 nanofibers. This work lays the foundation for outperformed hybrid electrode materials applied in energy conversion and storage.

Key Words: Metal oxides, nanostructures, energy conversion and storage, synergistic effect

DEDICATION

This thesis is dedicated to my parents, Ms. Xia Zhang and Mr. Guoqiang Sun, who have been guiding, supporting, encouraging, and inspiring me as two of my best friends throughout my life. Thank you for doing all your best to explore my potentials and offer me the best conditions. I also want to dedicate this thesis to "the most important decision", my dear husband Mr. Qiang Li, who is always on my side and take care of me with all his heart. Without the love or support from them, this thesis can never be finished.

ACKNOWLEDGMENTS

First of all, I want to express my sincere gratitude to my advisor, Dr. Yuanbing Mao, Department of Chemistry at the University of Texas-Pan American (UTPA), for his excellent guidance, caring, and patience, for his contributions of time, ideas, and funding to make my research efficient. I appreciate all the support and encouragement from Dr. Karen Lozano, Department of Mechanical Engineering at UTPA, who has provided an excellent model role as a successful woman professor. I also thank my committee members Dr. Jose J. Gutierrez, Dr. Jason Parsons, and Dr. John R. Villarreal, for their valuable advice and understanding.

I especially want to thank Mr. Qiang Li, Department of Mechanical Engineering, for his excellent advice, collaboration and immense contribution in SEM, AFM, TGA, DSC and electrochemical data collection. I also would like to acknowledge Mr. Faraon Torres, Mr. Aleksey Altecor, and Mr. Alfonso Salinas for their SEM support and training. Professor Yinong Lv, Materials Science and Engineering Department at Nanjing University of Technology, and Dr. Jiechao Jiang, Materials Science and Engineering Department at the University of Texas at Alington offered me generous help with TEM and HRTEM characterization.

My group members have contributed greatly to my professional time and also personal life in UTPA. The group has been a source of friendships to me. I express my gratitudes to Mr. Suresh Babu Alaparthi, Dr. Jahangeer Ahmed, Dr. Lee Cremar, Dr. Baicheng Weng, Dr. Fenghua Xu, Mr. Eduardo Villarreal, Ms. Qianqian Lu, Mr. Long Lu, Ms. Jessica Cruz, and Ms. Edna Garcia for their warm help and encouragement.

TABLE OF CONTENTS

Page

ABSTRACT iii
DEDICATION iv
ACKNOWLEDGEMENTS v
TABLE OF CONTENTS vi
LIST OF TABLES viii
LIST OF FIGURES ix
CHAPTER I. INTRODUCTION 1
  1.1 Background 1
  1.2 Nanostructured Electrode Materials 4
  1.3 Nanostructured Transition Metal Oxides 5
  1.4 Present Problems 6
  1.5 Main Solutions 6
  1.6 Proposal I-ZnO Nanoforests 7
  1.7 Proposal II-ZnO@MnO_2 Nanoforests 8
  1.8 Proposal II-V_2O_5@PPy Nanofibers 10
CHAPTER II. ZNO NANOFORESTS FOR ENERGY CONVERSION 13
  2.1 Introduction 13
  2.2 Experimental 16
    2.2.1 Growth of ZnO Nanowire Arrays 16
    2.2.2 Growth of ZnO Nanobranches onto the Preformed ZnO Nanowire Arrays 17
    2.2.3 Characterization 17
    2.2.4 Photoelectrochemical Measurements 19
  2.3 Results and Discussion 19
    2.3.1 Effect of Ammonia Concentration on the ZnO Branch Growth 20
    2.3.2 Effect of PEI Concentration on the ZnO Branch Growth 26

2.3.3 Synergistic Effect of Ammonia and PEI Concentrations on the ZnO Secondary Branch....29
2.3.4 Photoelectrochemical Water Splitting Performance of the ZnO Nanoforests........ 34
2.4 Conclusion.... 41
CHAPTER III. ZNO@MNO2 NANOFORESTS FOR ENERGY STORAGE.... 42
3.1 Introduction.... 42
3.2 Experimental.... 44
3.2.1 Materials.... 44
3.2.2 Preparation of 3-D ZnO@MnO$_2$ Core@shell Nanostructures.... 45
3.2.3 Characterization.... 46
3.2.4 Electrochemical Measurements.... 46
3.3 Results and Discussion.... 47
3.3.1 Morphology and Structure Characterization.... 47
3.3.2 Electrochemical Measurements.... 51
3.4 Conclusion.... 57
CHAPTER IV. V2O5@PPY NANOFIBERS FOR ENERGY STORAGE.... 58
4.1 Introduction.... 58
4.2 Experimental.... 60
4.2.1 Synthesis of V$_2$O$_5$ Nanofibers.... 60
4.2.2 Decoration of PPy on V$_2$O$_5$ Nanofibers.... 60
4.2.3 Characterization.... 61
4.2.4 Electrochemical Measurements.... 61
4.3 Results and Discussion.... 63
4.4 Conclusion.... 72
REFERENCES.... 73
BIOGRAPHICAL SKETCH.... 81

LIST OF TABLES

Page

Table 1: The main characteristics of LIBs and EDLCs..3

Table 2: Various PEI and ammonia concentrations used to control the growth of ZnO nanobranches onto the preformed ZnO nanowire arrays while keeping other growth conditions the same..18

Table 3: Discharging capacitance retention of the as-synthesized 3D ZnO@MnO_2 core@shell nanoforests and corresponding nanowire arrays at different current densities in the voltage range of -0.2 to 0.6 V (vs. Ag/AgCl)....................................56

Table 4: Specific capacitance of V_2O_5@PPy-x ratio at different scan rates.................................67

Table 5: Capacitance contributions for each V_2O_5@PPy composite...69

LIST OF FIGURES

Page

Figure 1.1: Schematic representation of a lithium-ion battery during discharging........................2

Figure 2.1: Illustration of the morphology and size evolutions of the ZnO nanobranches onto the preformed ZnO nanowire arrays to form the ZnO nanoforest by altering ammonia and PEI concentrations of the nutrient solution...20

Figure 2.2: SEM images of the obtained ZnO nanoforests after growing ZnO nanobranches onto the preformed ZnO nanowire arrays in precursor solutions with different concentrations of ammonia but without PEI. H: $c(NH_3{\cdot}H_2O) = 0$; HA1: $c(NH_3{\cdot}H_2O) = 0.03$ M; HA2: $c(NH_3{\cdot}H_2O) = 0.05$ M; HA3: $c(NH_3{\cdot}H_2O) = 0.10$ M; HA4: $c(NH_3{\cdot}H_2O) = 0.12$ M; and HA5: $c(NH_3{\cdot}H_2O) = 0.15$ M. Panels (i) and (ii) represent side- and top-viewed SEM images with different magnifications.............23

Figure 2.3: (A) XRD patterns of the ZnO nanoforest samples from H to HA5. (B) Variations of the calculated Harris's texture coefficient, T_c, for 0002, $10\bar{1}0$, and $10\bar{1}1$ diffractions based on the XRD patterns shown in (A)..24

Figure 2.4: SEM images of the obtained ZnO nanoforests after growing ZnO nanobranches onto the preformed ZnO nanowire arrays in precursor solutions with no ammonia but different concentrations of PEI. HP1: $c(PEI) = 0.0035$ M; HP2: $c(PEI) = 0.005$ M; and HP3: $c(PEI) = 0.007$ M...28

Figure 2.5: (A) XRD patterns of samples H, HP1, HP2 and HP3. (B) Variations of the calculated Harris's texture coefficient, T_c, for 0002, $10\bar{1}0$, and $10\bar{1}1$ diffractions based on the XRD patterns in (A)..29

Figure 2.6: SEM images of ZnO nanoforest after growing ZnO nanobranches onto the preformed ZnO nanowire arrays from the precursor solution with 0.15 M of ammonia and varying concentrations of PEI. HAP1: c(PEI) = 0.0035 M; HAP2: c(PEI) = 0.005 M; HAP3: c(PEI) = 0.007 M..30

Figure 2.7: (A) XRD patterns of samples HA5, HAP1, HAP2 and HAP3. (B) Variations of the calculated Harris's texture coefficient T_c for 0002, $10\bar{1}0$ and $10\bar{1}1$ diffractions based on the XRD patterns shown in (A)...31

Figure 2.8: (A) SEM, (B) TEM image and (C) SAED pattern of an individual ZnO nanotree of sample HA5. (D) HRTEM image and SAED (inset) of a branch from the ZnO nanotree shown in (A-C). (E) SEM, (F) TEM image and (G) SAED pattern of a willow-like ZnO nanotree of sample HAP3. (H) HRTEM image and SAED pattern of a branch from the willow-like ZnO nanotree shown in (E-G)...................33

Figure 2.9: (A) Photocurrent density-potential curves; (B) photoconversion efficiency; (C) impedance spectra; (D) response of V_{oc}; and (E) photoelectron lifetime from three nanostructured ZnO architectures: nanowire arrays, short-branched nanoforest, and willow-like nanoforest. (F) Schematic model displaying the illuminated photoanode to explain the enhanced charge transport and light trapping in willow-like ZnO nanoforest..36

Figure 3.1: Schematic illustration of the fabrication process for the designed 3-D ZnO@MnO$_2$ core@shell nanowire array electrode and its nanoforest counterpart. The latter possesses further boosted electrochemical performance than the former......43

Figure 3.2: Typical SEM images of (A, B) ZnO@MnO_2 nanowire arrays and (C, D) ZnO@MnO_2 nanoforests......48

Figure 3.3: Representative TEM and HRTEM images of the synthesized 3-D ZnO@MnO_2 core@shell (A and B) nanowire arrays and (C and D) Nanoforests......49

Figure 3.4: Detailed XPS data taken from the synthesized 3D ZnO@MnO_2 core@shell nanoforests: (a) the spectrum of Zn 2*p*. (b) the spectrum of Mn 2*p*......49

Figure 3.5: Overview XPS spectrum of the as-synthesized 3D ZnO@MnO_2 core@shell nanoforests......50

Figure 3.6: Energy-dispersive X-ray spectroscopy (EDS) data taken from the as-synthesized 3D ZnO@MnO_2 core@shell nanoforests shown in Figure 3.3c......50

Figure 3.7: SAED patterns of the as-synthesized 3D ZnO@MnO_2 core@shell (a) nanowire arrays and (b) nanoforests......51

Figure 3.8: (a) Cyclic Voltammetry (CV) curves of ZnO@MnO_2 nanforest electrode at different scan rates. (b) CV curves of the 3-D ZnO@MnO_2 nanoforests, ZnO@MnO_2 nanowire arrays, and titanium substrate as working electrodes at 2 mV s^{-1}......52

Figure 3.9: Cyclic Voltammetry (CV) curves of the as-synthesized 3D ZnO@MnO_2 nanowire arrays as the working electrode at different scan rates......53

Figure 3.10: (a) Charge/discharge (CD) curves of 3-D ZnO@MnO_2 nanoforests as electrode at different current densities; (b) Charge/discharge (CD) curves of ZnO@MnO_2 nanowire arrays as electrode at different current densities; (c) CD curves of

$ZnO@MnO_2$ nanowire arrays and nanoforests as working electrodes, respectively, at current density of 0.02 mA cm^{-2}; (d) Specific capacitances of $ZnO@MnO_2$ nanoforest and nanowire arrays at different current densities..................................54

Figure 4.1: (A) Raman spectra and (B) XRD patterns of V_2O_5 NFs and V_2O_5@PPy..................63

Figure 4.2: (A) SEM image of as prepared V_2O_5 nanofibers; (B) SEM image of as-prepared V_2O_5@PPy; (C) & (D) TEM and HRTEM images of as-prepared V_2O_5@PPy........64

Figure 4.3: TGA curves of V_2O_5 with different ratios of PPy coatings.......................................65

Figure 4.4: Cyclic Voltammetry curves of V_2O_5 coated with different mass ratios of PPy/V_2O_5 at scan rates of 0.5~500 mV/s: (A) V_2O_5@PPy-0%, (B) V_2O_5@PPy-5%, (C) V_2O_5@PPy-10%, (D) V_2O_5@PPy-30%, (E) V_2O_5@PPy-40%, (F) EDS pattern of as-prepared V2O5@PPy-50%...65

Figure 4.5: (A) Rate capability of V_2O_5@PPy composites with different ratios of PPy/V_2O_5 at scan rates of 0.5~500 mV/s; (B) cyclic voltammetry (CV) curves of corresponding V_2O_5@PPy composites at scan rate of 10 mV/s...............................66

Figure 4.6: (A) Rate capability of V_2O_5@PPy composites arising from CD measurements at different current densities; (B) Rate capability of V_2O_5@PPy composites with different ratios of PPy/V_2O_5 at 0.2 A/g and 1.0 A/g, respectively............................69

Figure 4.7: Nyquist plots for V_2O_5@PPy composites with different mass ratios of PPy/V_2O_5: 0%, 5%, 10% 30%, 35%, 40%, 50%...70

Figure 4.8: Digital pictures of V_2O_5@PPy composites with different mass ratios of PPy/V_2O_5: 0%, 5%, 10% 30%, 35%, 40%, 50%...71

CHAPTER I

INTRODUCTION

1.1 Background

With the depletion of non-renewable resources, environmental pollution and global warming increasing dependence on fossil fuels in the modern civilization, our society urgently needs scientists and engineers to develop sustainable, renewable and environmentally friendly energy substitutions. Although people already realized the considerable potential value of renewable energy production from solar and wind, their restricted applications are driving more of our attentions to developing more efficient and controllable energy conversion and storage systems.

Energy conversion system here is to convert solar energy into chemical energy by photocatalyst splitting water to generate hydrogen and oxygen, which has been widely considered as a promising idea.[1-2] Under solar radiation, photocatalyst such as ZnO or TiO_2 generates electrons, which are transferred through external circuit and reduce H^+ ions into H_2. Meanwhile, the holes produced by photocatalyst move through the materials onto the surface and oxidize O^{2-} ions into O_2. Therefore, photocatalyst is the essential element in energy conversion system.

While for energy storage system, the two key systems leading the state-of-the art are lithium-ion batteries (LIBs) and electrochemical capacitors (ECs), which are playing a crucial role in our daily life to power portable electronics such as cell phones, laptops, digital cameras. However, those systems still cannot fulfill the current and future needs from the society, such as electric vehicles and large-scale electrical grids, especially in the field of microelectromechanical systems (MEMS).[3-4] In spite of different definitions, both of LIBs and ECs, in essence, belong to electrochemical energy storage devices and have many similarities in configuration. Generally, an integrated LIB or EC system consists of three indispensable parts, a negative electrode (anode), a positive electrode (cathode), and an aqueous/non-aqueous electrolyte (shown in Fig. 1). The electrolyte could be liquid or solid. Solid electrolyte is usually applied with gaseous or liquid electrodes; while solid electrodes separated by a liquid electrolyte are kept apart by an electrolyte-permeable separator. On charging, cations (Li^+, Na^+, K^+, H^+, etc.) or anions (OH^-, etc.) coming from either one electrode or electrolyte move across the electrolyte and adsorb onto/insert into the other electrode, achieving polarization of the electrochemical system. Reversibly, the discharge is a depolarization process wherein ions spontaneously desorb/extract from the electrode and return to the other one. The electrons, in the meantime, pass around the external circuit.

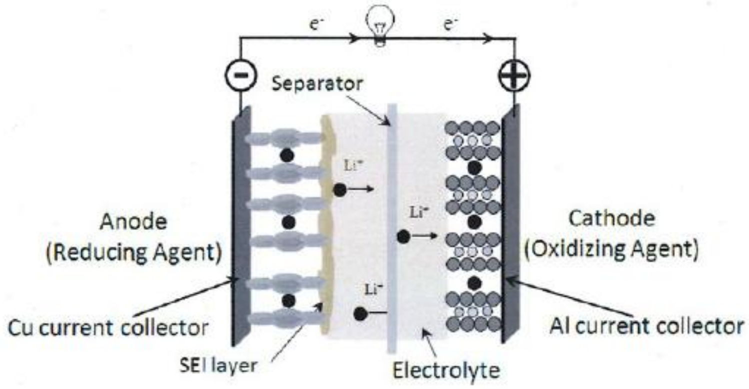

Figure 1.1 Schematic representation of a lithium-ion battery during discharging.[5]

Despite of many common features, LIBs and ECs also have some differences in the charge storage mechanism. Based on the charge storage mechanism and the active materials, ECs can be distinguished into two main types: electric double layer capacitors (EDLCs), and pseudocapacitors. EDLCs, as the most common device at present, utilize carbon-based active materials with high surface area. Pseudocapacitors use transition oxides (such as RuO_2, Fe_3O_4, NiO, and MnO_2) and/or electrically conductive polymers as electroactive materials (such as polyanilines, polypyrroles, and polythiophenes).[6] Both of the two EC systems store charges only at the surface or in a thin-layer region of active materials (several tens of nanometers from the surface) by means of adsorption/desorption of ions to form electric double layers or using reversible surface/near-surface faradic reactions.[6-7] Therefore, ECs can provide high charge/discharge capabilities (leading to high power densities) because of the non-solid state ion diffusion while possessing poor energy density (~ 1-10 Wh kg^{-1}) caused by limited active surface areas (for EDLCs), or inadequate use of entire pseudocapacitive materials (for pseudocapacitors).

Table 1 The main characteristics of LIBs and EDLCs.

	Nature of energy storage	Charge time	Discharge time	Energy density (Wh kg^{-1})	Power density (kW kg^{-1})	Charge/discharge efficiency (%)	Cycle life
LIBs	Chemical	1-5 h	0.3-3 h	20-100	0.5-1	50-90	500-2000
EDLCs	Physical	1-30 s	1-30 s	1-10	5-10	75-95	>500000

The basic characteristics of LIBs and ECs especially EDLCs, are compared in the Table 1. LIBs can theoretically store charge by the intercalation of Li^+ ions not only on the surface but also into the bulk of active materials. As a result of storing energy in a chemical form, LIBs are capable of delivering a much higher energy density (~20-100 Wh kg^{-1}, in some cases two orders of magnitude higher than that of ECs). But LIBs are suffering from relatively low power density, because of their formidable kinetic problems and slow diffusion of Li^+ ions in solid bulk materials. The high-efficiency energy storage needs these devices to possess the ability to store large quantities of electrical energy in small space and release the energy rapidly, which would never be realized without rational design of appropriate electrode materials.

1.2 Nanostructured Electrode Materials

Although proper choice of electrolytes with excellent ionic conductivity and electrochemical stability are very important to energy conversion and storage system, the performances of those devices mainly depend on the nature of electrode materials and their rational designs of material combination, morphology and size.[7] As the micrometer-sized bulk materials have already reached their intrinsic limit and failed to meet the increasing energy demand, various nanostructured materials are being researched in recent years.[8]

The evolution of nanostructured materials has greatly promoted the development of energy storage devices, because these nanomaterials possess some advantages over their bulk counterparts. Firstly, nanostructured materials can be designed to have a very high surface area, which leads to an enhanced specific capacitance or capability. Secondly, the extremely small particle size of nanomaterials can significantly shorten the path length of ion transfer and dramatically enhance the charge/discharge rate. In addition, small particle size can release stress from the expansion and contraction of crystalline electrodes during charge/discharge process, improving the cycle stability. Thirdly, nanomaterials can be designed to be structurally uniform and possess controllable morphologies, which both are very important to the transport of electrolyte ions and their real applications.[9]

1.3 Nanostructured Transition Metal Oxides

Although the carbon-based active materials have been widely used in commercial LIB and EC devices, their performances still need further enhancements. Thus more and more researchers are searching for alternative electrodes. Among various candidates, transition metal oxides (M_xO_y, such as Fe_3O_4, NiO, Co_3O_4, V_2O_5 and MnO_2), especially in the form of nanomaterials, have attracted great interest due to their low cost, environmentally friendly synthesis processes, and their rich redox reactions involving different ions, which contributes to high specific capacities/capacitance (in general multiple times higher than those of carbon/graphite-based materials). In addition, some metal oxides such as MnO_2 are abundant in nature and thus low-cost. The size, morphology, orientation and crystallinity of metal oxide nanostructures can also be easily tuned, which makes it possible to systematically investigate the structure-electrochemical property relationships.[10]

However, the use of metal oxides also brings several unpleasant difficulties as discussed blow. Firstly, most of the extensively studied oxides belong to wide bandgap semiconductors or even insulators. So they usually exhibit poor electrical conductivity, which restricts power delivery on the few seconds time scale and will possibly causes safety problems during repeated charge/discharge operations. Secondly, metal oxides would generally suffer from poor ion transport kinetics. While downsizing oxides into nanoscale and/or making hierarchically porous structures can facilitate ions to enter the inner side of the electrode matrix by offering sufficient ion transport pathways, they would at the same time inevitably cause the increase electrical resistance in the solid electrode due to increases amount of grain boundaries. Thirdly, especially for LIBs, metal oxides inevitably suffer from pronounced volume expansion and contraction during charging/discharging processes, resulting in the pulverization of electrode film.

1.4 Present Problems

Due to their intrinsic material properties, such as low conductivity, weak mechanical stability and associated side reactions (caused by un-protected surfaces), single-phase nanomaterials are not able to meet the current needs from the society. Especially in the field of microbatteries, the inability of electrochemical power sources is extremely apparent, which means battery miniaturization has not kept pace with advances in the development of MEMS. The size of those devices is determined by the size of their power supply, and integrating the power supply within the device structure is not possible because of the small size of the device.

1.5 Main Solutions

In order to surpass those limitations associated with single phased nanomaterials, various hybrid nanostructured electrode material systems have been proposed with rational design and elegant architectures.

Hybrid nanostructures can be described as a combination of two or more components which have been thoroughly researched in their respective fields but deliver enhanced properties or novel useful properties in becoming part of the hybrid combination. The ability of designing various hybrid nanomaterials completely depends on the internal and external interfacing capabilities and also on the physical/chemical compatibility of individual components.

The application of nanostructured hybrid electrode materials represents a promising direction to boost the electrochemical performance of metal oxides, because of the following advantages. Superior to single phased materials, the hybrid systems integrate several types of functional materials which can synergistically enhance the intrinsic properties of each component such as electrical/ionic conductivity, electrochemical reactivity, and mechanical stability. Moreover, from the viewpoint of surface electrochemistry, a hybrid design such as core@shell structure, can effectively decrease the surface energy of the active nanomaterials. This protects against side reactions between the electrode and electrolyte that would cause a high level of electrochemical irreversibility, and at the same time avoids particulate aggregation that may lead to poor cycle stability.

1.6 Proposal I-ZnO Nanoforests

To develop better photoelectrodes and more efficient devices, one of the main strategies is the nanostructuring strategy by exploiting scaling laws and specific effects at the nanoscale to enhance the efficiency of existing semiconductors and metal oxides. Moreover, compared with 1D nanowire arrays, three-dimensional (3D) branched ZnO nanotree arrays, i.e. nanoforest, have recently demonstrated their more marvelous performances and promising potentials in various applications, especially energy conversion and storage. The energy conversion efficiency of dye-sensitized solar cells (DSSCs) can also be improved by about five times after branching ZnO nanowire arrays.[11] These surprising progresses are derived from the fascinating 3D branched

ZnO nanotree configuration, not only inheriting the advantages of nanowire arrays (e.g. shorter diffusion path for carrier transport), but also achieving largely augmented surface area within a given footprint. Furthermore, 3D ZnO nanoforests have not been explored as photoanodes in photoelectrochemical (PEC) cells for hydrogen generation from water splitting despite their aforementioned successful demonstrations in supercapacitors and DSSCs.[12]

Therefore, we propose to conduct morphology-programmed hydrothermal synthesis to fabricate 3D branched nanotree arrays with well-defined shape and size. The main significance of this research for tailoring the morphology and size of 3D branched ZnO nanotree arrays is to adjust the hydrolysis rate, nucleation speed, and supersaturation degree of zinc ions by controlling the potential of hydrogen (pH) value and aggregation of surfactant in the reaction solution, more specifically, the concentration of ammonia and/or PEI. Other than offering a highly enhanced surface area on limited footprint, the as-fabricated ZnO nanoforest also builds a 3D interconnected matrix structure with shorten carrier collection pathways, good electrical conductivity, and improved light absorption, which are expected to substantially benefit the PEC performance.

1.7 Proposal II-ZnO@MnO_2 Nanoforests

For the small-sized autonomous devices, a key consideration for miniaturization, especially for integrated power, is the footprint area of the devices. Traditional battery designs with 2D geometries need large footprint areas to achieve large capacities. While making electrodes thicker in the same foortprint to store more energy is not a wise option, because the mechanical integrity of the film decreases with thickness and also because thicker film reduce the power density of devices. In general, 2D battery designs result in a compromise between energy density and power density because of the limitation in footprint area.[3]

With emergence of 3D battery architectures which can increase the amount of electrode material within a given footprint area, the power density and energy density of microbatteries and microcapacitors could be decoupled. Compared with compact two-dimensional (2D) counterparts, 3D architectures take advantage of the vertical dimension-height, possessing higher surface/body ratios, larger surface areas, more surface active sites within a small footprint area, and accordingly enlarged areal capacity. Besides, compared to disordered ones, ordered 3D arrays of hybrid nanostructures have advantages of efficient electron transfer between current collector support and individual electrode material and fast ion transport/easy electrolyte access to electrode due to available void volume between adjacent nanostructured electrodes. Further, the void volume in the ordered hybrid electrode arrays helps in accommodating volume expansion of the material. Therefore, 3D ordered hybrid nanomaterials have been prepared for more efficiently powering MEMS and other small autonomous devices.[3, 8]

Some efforts have been devoted to engineering 3D nanostructures as electrochemical energy storage electrodes. For examples, Liu *et al.* built electrodes made of Co_3O_4@MnO_2 nanowire arrays through sacrificial reactive 3D carbon template layers.[13] Xia *et al.* synthesized Co_3O_4@NiO core@shell nanowire arrays for supercapacitors with outstanding high capacitance and good cycling stability.[14] All these 3D core@shell heterostructures discussed here consist of high conductive 1D nanowires as the core and electroactive transition metal oxide/hydroxide as the shell. In this manuscript, inspired by branched trees with larger surface area to capture more sunlight,[11] we postulated that novel electrode architecture composed of branched nanowire arrays, i.e. forest of nanotrees, could possess further boosted electrochemical performance over that of 1D nanowire arrays. To our best knowledge, no electrodes composed of nanoforests have been applied to electrochemical energy storage devices yet.

Therefore, we propose to fabricate ZnO@MnO_2 core@shell nanowire arrays and nanoforests as electrode materials, following the steps of Scheme 1, and compare their electrochemical performances applied in energy storage devices. Not only because the 3D ZnO nanotree backbone with high specific area provides highly conductive channels to effective electron transport like “highways”; also, MnO_2 as a promising candidate with low-cost, abundance, high theoretical capability and environmental friendliness, has been widely studied in LIB and ECs. We believe this new design not only can fill the void in the gallery of heterostructured nanomaterials with 3D skeleton applied in energy storage devices, but also provide a direction to meet the miniaturization requirements of powering MEMS and other functional small devices.

1.8 Proposal III-V_2O_5@PPy Nanofibers

Vanadium oxide (V_2O_5) has been extensively studied in diverse fields including catalysis, sensors, electrochromic devices, and more recently in LIBs and ECs, because of the ease to accommodate molecules or ions into its layered structure and high energy density, and wide potential window arising from its various vanadium oxidation states (V-II).[15] As a cathode material for LIBs, V_2O_5 can deliver a theoretical capacity of 440 mA h/g based on intercalation of three Li^+ ions, which is about twice higher than that of traditional electrode materials, for example with $LiCoO_2$ (140 mA h/g) and $LiFePO_4$ (170 mA h/g). However, the development of V_2O_5 electrodes in LIBs and ECs has been limited by its poor structural stability, low electronic conductivity, slow electrochemical kinetics, and high dissolution of vanadium ions. Those drawbacks are very detrimental to high-rate and long-term cycling performances of devices.

Recently, many researchers have developed some strategies to enhance the electron diffusion rate of V_2O_5, such as doping foreign atoms into V_2O_5 or integrating V_2O_5 with high electronically conductive materials. Xiong *et al.* introduced Ag atoms into V_2O_5 nanowires to enlarge electrical conductivity interlayer spacing for electrochromics.[16] Yan *et al.* coated V_2O_5 on SnO_2 nanowires to obtain high-power-density and high-energy density LIBs.[17] Chen *et al.* deposited V_2O_5 on mutiwall carbon nanotube (MWCNT) sponge backbone to serve as a high-performance cathode in LIBs.[18] Although these strategies can effectively improve electronic transport, they are still not able to prevent vanadium dissolution, which results in low cycling stability.

On the other side, conducting polymers (e.g., polyaniline (PANI), poly(3,4-ethylenedioxythiophene) (PEDOT), Polypyrrole (PPy), etc.) are also considered as a category of promising supplementary materials to couple with metal oxides for advanced electrochemical energy storage. The advantages of conducting polymers mainly include the ease of synthesis, relatively high electronic/ionic conductivity and the feasibility of forming uniform and highly porous film. Besides, conducting polymers having well-defined redox behavior can also function as good electrode materials. As a result, the combination of conducting polymers and metal oxides would provide some superiority especially for the LIB application. The hybrid of conductive polymers with metal oxides especially its decoration on metal oxides, can not only lead to the synergetic effects between polymer and oxides, but also offer a flexible buffering layer, increase the conductivity of electrodes, greatly improving the battery lifetime and often enhancing the rate performance to some extent. Among the conducting polymers, polypyrrole

(PPy) has been widely studied as a part of electrode materials, owing to its good chemical and thermal stabilities, easy synthesis, high specific capacitance, and high electrical conductivity.[19]

In our proposal, electrical conductive polymer PPy will be uniformly grown on the surface of layer-structured V_2O_5 nanofibers, to work as electrode materials in LIBs and ECs. The obtained core@shell structured V_2O_5@PPy nanocomposites are expected to resolve the above two problems simultaneously utilizing the electronic conductivity and polymeric coating effect of PPy to protect vanadium ions from dissolving into aqueous electrolyte. Besides, optimization of the ratio of PPy to V_2O_5 will be explored, expecting to obtain the highest electrochemical performances for V_2O_5@PPy electrode materials.

CHAPTER II

ZNO NANOFORESTS FOR ENERGY CONVERSION

2.1 Introduction

Rational design and control over the morphology and function of inorganic crystals is a long-standing goal in materials science and engineering.[20] Various nanostructures with desirable morphologies have attracted broad attention because of their fantastic interior architectures and variation in the physicochemical properties caused by interfacial effects. These features play pivotal roles in determining nanomaterials' properties and can lead to many potential applications. Therefore, morphology-programmed and controlled synthesis with a predictive model based on morphology-property relationship will greatly advance materials science and nanotechnology while it remains as a significant challenge and in an urgent need.[21-24]

At the meantime, sunlight is an abundant, inexpensive, pollution-free and endlessly renewable source of clean energy. Converting solar energy into an easily usable form has attracted considerable interest in the last several decades. Among different technologies for solar energy conversion, photoelectrolysis has been used to split water in hydrogen and oxygen without any emission of byproducts. However, the conversion efficiency today remains low (e.g. lower than that of photovoltaics), and is limited mainly by the low performance of the photoelectrodes. To develop better photoelectrodes and more efficient devices, one of the main strategies is the nanostructuring strategy by exploiting scaling laws and specific effects at the nanoscale to enhance the efficiency of existing semiconductors and metal oxides. This has gained significant interest in the last twenty years.[5]

Among existing semiconductors and metal oxides, zinc oxide (ZnO) has been one of the most favorable materials. It has been widely applied in electronics, sensors, catalysts, and more recently energy conversion/storage devices due to its excellent stability, environmental friendliness and low cost.[12, 25-30] Therefore, morphology-tunable synthesis of ZnO nanostructures is substantially crucial for exploring their further potentials and for enabling scientists with great manipulation power on material and device performance.[23, 31-32]

There are manifold synthesis methods reported in the literature for ZnO nanostructures, including hydrothermal synthesis,[27, 33] vapor-liquid-solid (VLS) process,[32] chemical vapor deposition (CVD),[34] and microwave irradiation synthesis.[31] Among these well-accepted growth strategies, hydrothermal synthesis stands out and has successfully promoted bottom-up nanoscience to a new level due to its low cost, low synthesis temperature, easy scaling up, and environmental benignity.[35] Through introducing and altering different capping agents with preferential binding abilities on different ZnO crystal surfaces, hydrothermal synthesis possesses the capability to systematically manipulate and creatively grow ZnO nanostructures into diverse forms, such as nanorods, nanowires, nanotubes, nanoflowers, and nanotrees.[11, 26-27, 33, 36-37] On the long list of its splendid architectures, one-dimensional (1D) ZnO nanowire arrays were considered as one of the most significant morphologies.[26, 38] Also, numerous reports have studied the morphology-controlled growth of ZnO nanowire arrays through hydrothermal method by exploring the dependence between shape transition of its nanowire arrays and synthesis parameters, such as ammonia ($NH_3 \cdot H_2O$) and polyethylenimine (PEI).[20, 37, 39-42] Moreover, compared with 1D nanowire arrays, three-dimensional (3D) branched ZnO nanotree arrays, i.e.

nanoforest, have recently demonstrated their more marvelous performances and promising potentials in various applications, especially energy conversion and storage. For example, our group demonstrated that ZnO@MnO_2 nanoforest can generate five times higher areal capacitance than the nanowire array counterparts.[12] The energy conversion efficiency of dye-sensitized solar cells (DSSCs) can also be improved by about five times after branching ZnO nanowire arrays.[11] These surprising progresses are derived from the fascinating 3D branched ZnO nanotree configuration, not only inheriting the advantages of nanowire arrays (e.g. shorter diffusion path for carrier transport), but also achieving largely augmented surface area within a given footprint.

Similar to trees in the natural world by exposing sufficient surfaces of leaves and branches for effective photosynthesis, these branched nanostructures are expected to possess larger surface area to harvest solar light for photoelectrochemical and photocatalytic water splitting. They also cause increased scattering to improve light absorption. Moreover, they inherit the advantages of nanostructures, such as shortened carrier collection pathways, surface area-enhanced charge transfer, potential determining ions, and quantum size confinement among others.[2] However, there is no report yet in the literature on how to fine tune and control the morphology of 3D ZnO nanotree arrays via engineering the hydrothermal synthesis parameters. This limits our capability to regulate and design complex 3D configurations via hydrothermal approach.[43] It is extremely critical for advancing this powerful fabrication approach into a versatile nanomanufacturing technology. Therefore, in-depth investigation of shape-evolution of 3D ZnO nanoforests via hydrothermal growth is urgently desired. Furthermore, 3D ZnO nanoforests have not been explored as photoanodes in photoelectrochemical (PEC) cells for hydrogen generation from water splitting despite their aforementioned successful demonstrations in supercapacitors and DSSCs.[12]

To fill these voids, our group conducted morphology-programmed hydrothermal synthesis to fabricate 3D branched nanotree arrays with well-defined shape and size. The main significance of this research for tailoring the morphology and size of 3D branched ZnO nanotree arrays is to adjust the hydrolysis rate, nucleation speed, and supersaturation degree of zinc ions by controlling the potential of hydrogen (pH) value and aggregation of surfactant in the reaction solution, more specifically, the concentration of ammonia and/or PEI. Other than offering a highly enhanced surface area on limited footprint, the as-fabricated ZnO nanoforest also builds a 3D interconnected matrix structure with shorten carrier collection pathways, good electrical conductivity, and improved light absorption, which are proved to substantially benefit the PEC performance. From our measurements, the willow-like nanoforests led in PEC water splitting performance, and brush-like nanoforests surpassed nanowire arrays. Therefore, this work contributes to both scientific and technological fields because this economical low temperature fabrication technique holds extraordinary significances for large-scale solution processing of 3D hierarchical nanostructures, and the resulting nanoforest is expected to inspire a new general paradigm for various energy related applications.[3]

2.2 Experimental

2.2.1 Growth of ZnO Nanowire Arrays

As we previously reported, a seed solution of ZnO nanoparticles (Figure S1) was prepared by adding 25 mL of 0.03 M sodium hydroxide (NaOH) ethanol solution into 37.5 mL of

0.01 M zinc acetate [$Zn(O_2CCH_3)_2 \cdot 2H_2O$] ethanol solution drop by drop, and then the mixture was actively stirred at 60 °C for 2 h.[12] After that, the seed solution was drop casted onto indium tin oxide (ITO) glass substrates. ZnO nanowire arrays were grown from the ZnO nanoparticle seeds through immersing in an aqueous precursor solution consisting of 0.025 M zinc nitrate hydrate [$Zn(NO_3)_2 \cdot 6H_2O$], 0.025 M hexamethylenetetramine ($C_6H_{12}N_4$, HMTA), 0.05 M ammonia, and 0.0035 M PEI and heated at 60-90 °C for 7 h. The grown ZnO nanowire arrays were thoroughly rinsed with deionized water, and then dried in air (Figure S2).

2.2.2 Growth of ZnO Nanobranches onto the Preformed ZnO Nanowire Arrays

To develop the desirable 3D ZnO nanoforests, ZnO nanoparticle seed solution was first added onto the surface of the preformed ZnO nanowire arrays by a similar drop casting process, and subsequently a similar hydrothermal reaction was conducted as described above. To fine tune the growth of different ZnO branches onto the ZnO nanowire array trunks, the concentrations of ammonia and PEI were varied and controlled (Table 1). To remove residual organics (mostly PEI), the as-prepared ZnO nanostructures were annealed at 350 °C in air for 10 min. After annealing, they were also ensured excellent electrical conductivity, mechanical stability, and firm adherence onto the ITO substrate.[44]

2.2.3 Characterization

The morphology, chemical composition, and crystal structure of the seeded substrate, as-prepared ZnO nanowire arrays and nanoforests were characterized through atomic force microscopy (AFM), scanning electron microscopy (SEM), powder X-ray diffraction (XRD), Raman spectroscopy, transmission electron microscopy (TEM), high-resolution TEM (HRTEM), selected area electron diffraction (SAED) and energy dispersive X-ray spectroscopy (EDS).

AFM images of seeded substrate were taken with a Dimension 3000 AFM on TMC VT102 vibration isolation table at tapping mode. XRD analysis of the as-prepared ZnO nanoarchitectures was carried out using a Bruker AXS D8 QUEST diffractometer with Cu Kα radiation (λ = 1.5406 Å) between 25° and 70°. Raman spectroscopy was conducted on a Bruker SENTERRA RAMAN microscope with a 785 nm laser as the excitation source. XRD, Raman and SEM measurements were conducted directly with the as-prepared ZnO nanostructures on the ITO substrate. For SEM imaging, the ITO glass substrate with as-prepared ZnO nanostructures were attached directly onto the surface of SEM brass stub through conductive carbon tape using a Carl Zeiss Sigma VP Field-Emission SEM at 2-5 kV. TEM, HRTEM, SAED and EDS were carried out on a Hitachi H-9500 microscope with an accelerating voltage of 300 kV. Specimens for these studies were prepared by sonicating the as-prepared ZnO nanoforest on the ITO substrate in deionized water, followed by depositing a drop of the obtained suspension onto a 300 mesh Cu grid, coated with a lacey carbon film.

Table 2 Various PEI and ammonia concentrations used to control the growth of ZnO nanobranches onto the preformed ZnO nanowire arrays while keeping other growth conditions the same.

	Sample	[$NH_3{\cdot}H_2O$] [mol·L^{-1}]	[PEI] [mol·L^{-1}]
Control	H	0	0
Effect of [PEI]	HA1	0.03	0
	HA2	0.05	
	HA3	0.10	
	HA4	0.12	
	HA5	0.15	
Effect of [$NH_3{\cdot}H_2O$]	HP1	0	0.0035
	HP2		0.0050
	HP3		0.0070
Synergistic effect of [PEI] and [$NH_3{\cdot}H_2O$]	HAP1	0.15	0.0035
	HAP2		0.0050
	HAP3		0.0070

2.2.4 Photoelectrochemical Measurements

PEC measurements for water splitting were performed in a standard three-electrode electrochemical cell configuration, using the as-prepared ZnO nanoarchitectures grown on ITO glass as the working electrode, a platinum wire as the counter electrode, and Ag/AgCl as the reference electrode. A 0.5 M Na_2SO_4 solution buffered to pH ~7.0 with phosphate buffer solution was employed as the electrolyte and purged with N_2 for 5-10 min before the measurements. The PEC measurements, electrochemical impedance measurements, and open circuit voltage decay were recorded under AM 1.5 G illumination from a solar simulator (1 sun, 100 mV/cm^2, Iwasaki Solar Simulation Evaluation Systems equipped with EYE/Iwasaki electronic ballast system). The potential was measured against an Ag/AgCl reference and converted to reversible hydrogen electrode (RHE) potential by using the equation E(RHE) = E(Ag/AgCl) + 0.1976(V) + 0.059*pH.[45] All the PEC measurements were tested with illumination from the front side of the ITO glass substrate covered with the ZnO nanostructures. For each type of samples, tests were performed in triplicates in order to exclude the accidental phenomenon and prove reproducibility. Results from each type of samples agreed with each other.

2.3 Results and Discussion

Both the respective and synergistic influences of ammonia and PEI were systematically investigated on the morphology and size evolution of ZnO nanobranches onto the preformed ZnO nanowire arrays to form the ZnO nanoforest (Figure 2.1).

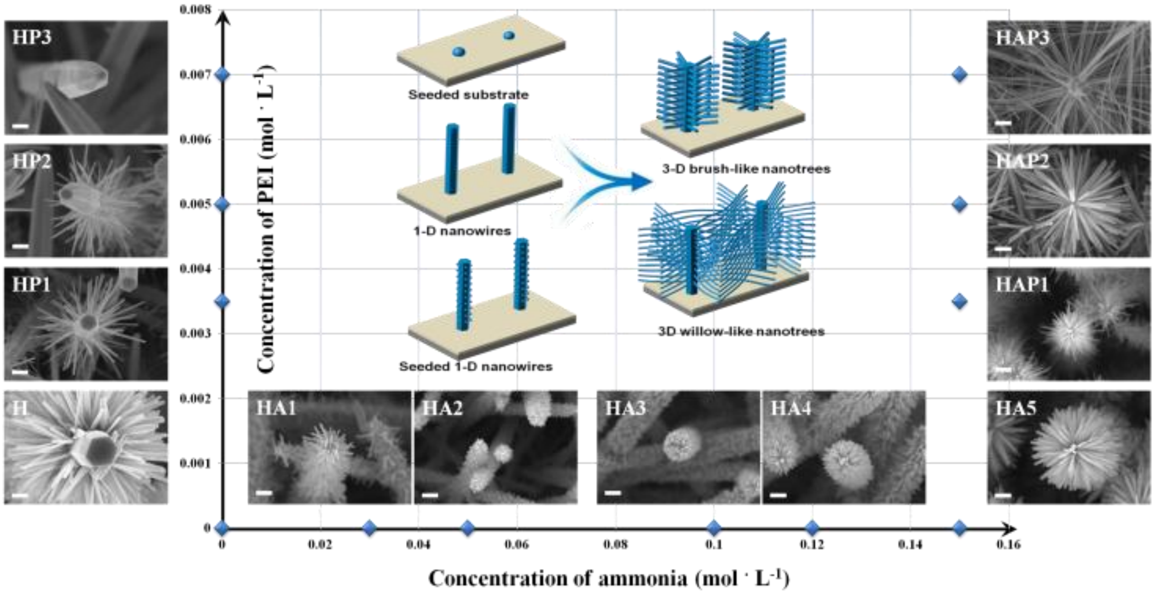

Figure 2.1 Illustration of the morphology and size evolutions of the ZnO nanobranches onto the preformed ZnO nanowire arrays to form the ZnO nanoforest by altering ammonia and PEI concentrations of the nutrient solution.

2.3.1 Effect of Ammonia Concentration on the ZnO Branch Growth

First, to understand how the preformed ZnO nanowire arrays transform and the ZnO nanobranches evolve under the influence of ammonia addition with different concentrations, the obtained ZnO nanostructures were studied using SEM (Figure 2) and XRD (Figure 3). The top- and side-viewed SEM images all clearly exhibit uniform ZnO nanoforests on large area with some changes on the ZnO trunks. These nanoforests are composed of oriented nanotrees uniformly rooted on the ITO glass substrate. Each of the trees consists of an upstanding trunk/stem and myriad side branches. Under closer look, these nanoforests prepared with different ammonia concentrations have different morphologies.

Apparently, the diverse nanoforests were originated from different precursor solution systems. Figure 2H revealed the ZnO nanoforest prepared from the preformed ZnO nanowire arrays in the nutrient $Zn(NO_3)_2$ and HMTA solution. $Zn(NO_3)_2$ and HMTA are the most commonly used chemical agents to hydrothermally synthesize ZnO nanowires. It is widely believed that besides the inherent fast growth along the direction of the polar surfaces of wurtzite ZnO, HMTA acts as a weak base and pH buffer, hydrolyzing in water and slowly releasing HCHO and NH_3.[28, 46] The following equations are involved in the formation of ZnO crystals in this solution:

$$\text{HMTA} + 6H_2O \rightleftharpoons 4NH_3 + 6HCHO \quad (1)$$

$$NH_3 \cdot H_2O \rightleftharpoons NH_4^+ + OH^- \quad (2)$$

$$Zn^{2+} + 2OH^- \rightleftharpoons Zn(OH)_2 \quad (3)$$

$$Zn(OH)_2 \rightleftharpoons ZnO + H_2O \quad (4)$$

Figure 2H demonstrates that the nutrient precursor solution composed of only $Zn(NO_3)_2$ and HMTA kept the trunks' top hexagonal shape and the trunks' top diameter around 200 nm. Relatively dense branches of averagely 650 ± 50 nm in length grew out along the trunk of ZnO nanotree. After introducing 0.03M ammonia into the nutrient solution, all the branches along the trunk immediately became shorter (~180 nm) and the top of the trunk was etched thinner (Figure 2HA1). With 0.05 M of ammonia, average branch length was further shorten to ~50 nm and the tip of trunk was barely observed due to the coverage by the short branches (Figure 2HA2). However, the growth of ZnO branches on the original ZnO nanowire arrays changed when the concentration of ammonia in precursor solution continued increasing. When the ammonia concentration increased to 0.10 M, both the diameter and length of the as-prepared ZnO nanobranches started to increase (Figure 2HA3). The petal-like branches are now ~90 nm long and compactly wrapped all over the trunks. With higher concentration of ammonia (i.e. 0.15 M), the branches were kept prolonging to around ~300 nm (Figure 2HA5).

Figure 3A displays the corresponding XRD patterns of ZnO nanoforests fabricated in different nutrient solutions with gradually increasing ammonia concentration. All the peaks belong to hexagonal wurtzite ZnO (JCPDS Card No. 36-1451) without any impure peaks. The peak positions are the same as the XRD pattern taken from the ZnO nanowire arrays before growing the ZnO branches (Figure S2A). As shown in Figure S2, the trunk of these ZnO nanoforests, i.e. the ZnO nanowire arrays, grow vertically from the ITO substrate along the direction of *c*-axis, so their strongest peak is the 0002 diffraction. For the ZnO nanoforest samples from H to HA5, their relative XRD peak intensities vary due to the altering concentration of ammonia. In Figure 3A, the intensities of the peaks at $(10\bar{1}0)$, $(10\bar{1}1)$, $(10\bar{1}2)$, $(11\bar{2}0)$, $(10\bar{1}3)$, $(11\bar{2}2)$, and $(20\bar{2}1)$ crystal planes are compared to the normalized (0002) peak intensity. Their relative intensities decreased first and then increased with increasing ammonia concentration in the precursor solutions for the growth of ZnO branches.

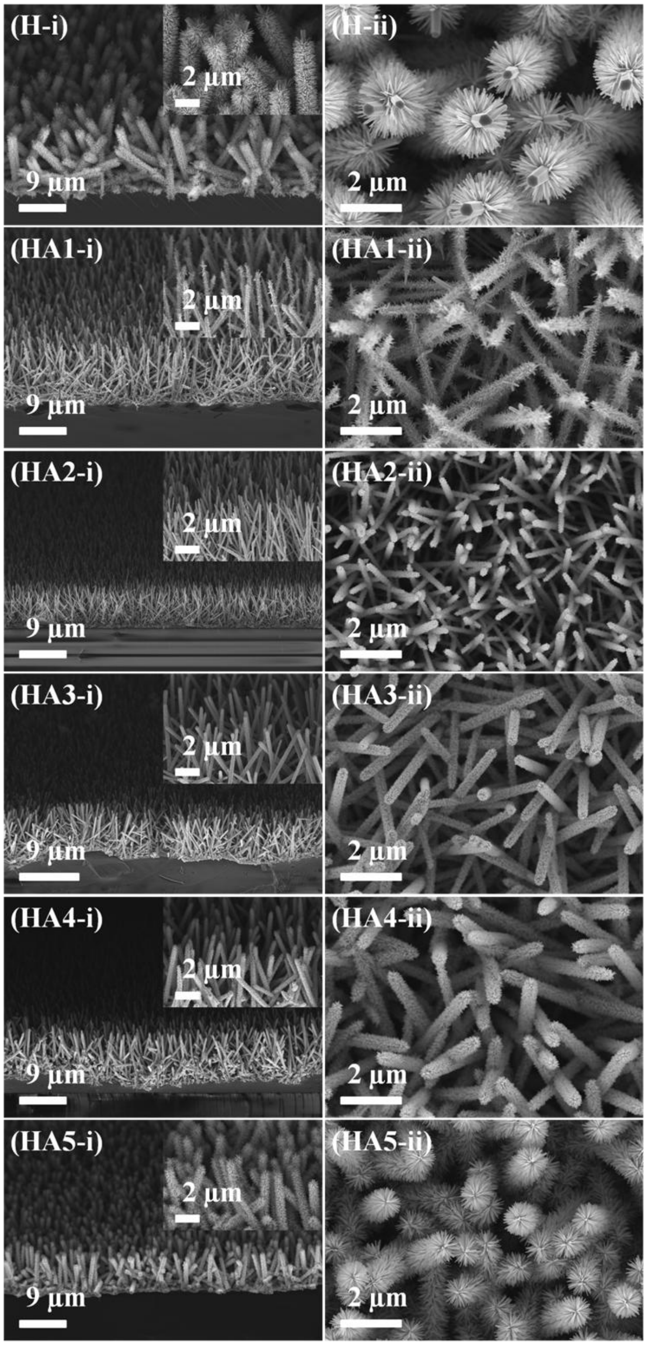
(H-i)
2 µm
9 µm
(H-ii)
2 µm
(HA1-i)
2 µm
9 µm
(HA1-ii)
2 µm
(HA2-i)
2 µm
9 µm
(HA2-ii)
2 µm
(HA3-i)
2 µm
9 µm
(HA3-ii)
2 µm
(HA4-i)
2 µm
9 µm
(HA4-ii)
2 µm
(HA5-i)
2 µm
9 µm
(HA5-ii)
2 µm

Figure 2.2 SEM images of the obtained ZnO nanoforests after growing ZnO nanobranches onto the preformed ZnO nanowire arrays in precursor solutions with different concentrations of ammonia but without PEI. H: $c(NH_3{\cdot}H_2O) = 0$; HA1: $c(NH_3{\cdot}H_2O) = 0.03$ M; HA2: $c(NH_3{\cdot}H_2O) = 0.05$ M; HA3: $c(NH_3{\cdot}H_2O) = 0.10$ M; HA4: $c(NH_3{\cdot}H_2O) = 0.12$ M; and HA5: $c(NH_3{\cdot}H_2O) =$

0.15 M. Panels (i) and (ii) represent side- and top-viewed SEM images with different magnifications.

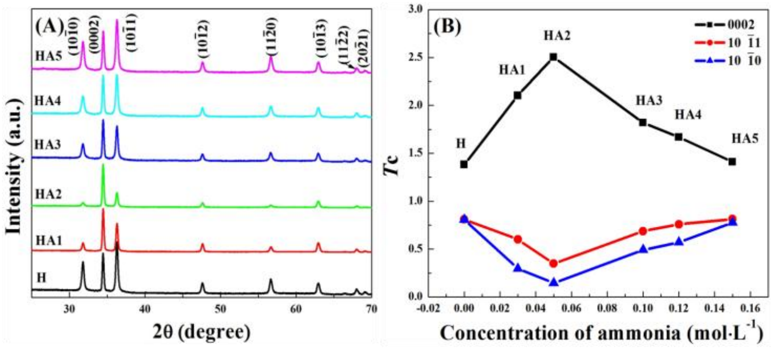

Figure 2.3 (A) XRD patterns of the ZnO nanoforest samples from H to HA5. (B) Variations of the calculated Harris's texture coefficient, T_c, for 0002, $10\bar{1}0$, and $10\bar{1}1$ diffractions based on the XRD patterns shown in (A).

The degree of crystallographic preferred orientation was estimated quantitatively by calculating Harris's texture coefficient, T_c.[40, 47] The T_c is defined as:

$$T_c(hkl) = n\frac{I_m(hkl)/I_0(hkl)}{\sum_1^n I_m(hkl)/I_0(hkl)} \tag{5}$$

where $I_m(hkl)$ is the measured relative intensity of the peak corresponding to the *hkl* diffraction, $I_0(hkl)$ is the relative intensity from the same diffraction in the standard powder sample (JCPDS Card No. 36-1451), and n is the total number of diffraction peaks considered in the evaluation. The T_c value ranges from 0 to n, and samples having a preferred (*hkl*) orientation and random orientation exhibit $T_c(hkl)$ values of ~n and ~1, respectively.

In the present case, we chose three diffractions ($n = 3$) of 0002, $10\bar{1}0$, and $10\bar{1}1$, and the results are plotted in Figure 2B. Easily notice that $T_c(0002)$ ascend firstly and then descend after sample HA2 with the increasing concentrations of ammonia, diametrical opposite of T_c values on the other two diffraction orientations. $T_c(0002)$ for sample HA2 is calculated to be ~2.505, similar to that of ZnO nanowire arrays ($T_c(0002) = 2.530$). Because the morphology of the HA2 nanoforest is the closest to that of the ZnO nanowire arrays, displaying the most apparent preferred orientation along <0002> direction and the minimum branch length (~50 nm, Figure 2HA2). While $T_c(0002)$ values of sample H and HA5 are respectively ~1.383 and 1.410, harmoniously approaching the situation of random orientation with $T_c = 1$, which is caused by the growth of random orientated long branches onto the ZnO nanowire arrays. The difference of T_c values between sample H and HA5 is attributed to bigger branches from the sample H, since crystalline volume can also affect the diffraction intensity.[40] On the other hand, both $T_c(10\bar{1}0)$ and $T_c\ (10\bar{1}1)$ are sharing the consistent trend with the branch length evolution from samples H to HA5 since the variation of T_c values is the result from both the orientation change and branch evolution of ZnO nanoforests.

Ammonia not only provides a basic environment, but also mediates the heterogeneous nucleation and growth of ZnO nanowires and branches. In our studies presented here, after 0.03 M ammonia was added into the system for sample HA1, the precursor solution immediately became turbid due to the rapid formation of white precipitate $Zn(OH)_2$ and ZnO through homogeneous nucleation. This process scrambles for free Zn^{2+} ions in the precursor solution, so the Zn^{2+} ions are depleted quickly. Under competing growth mechanism, it leads to early termination of the heterogeneous nanobranch growth onto the seeded preformed ZnO nanowire arrays, similar to that of the nanowire array growth onto the seeded substrate. Therefore, after introducing ammonia for sample HA1 and HA2, only petals were grown onto the ZnO nanowire arrays. When the ammonia concentration reached 0.10 and 0.15 M, the precursor solutions turned clear because sufficient ammonia can react with Zn^{2+} ions and generate soluble complex

$[Zn(NH_3)_4]^{2+}$. The introduction of adequate ammonia enhanced the solubility of zinc ions in the nutrient precursor, and also less precipitate was observed after the growth. The reversible reactions are shown in equations (6) and (7):

$$Zn^{2+} + 4NH_3 \rightleftharpoons [Zn(NH_3)_4]^{2+} \tag{6}$$

$$Zn(OH)_2 + 4NH_3 \rightleftharpoons [Zn(NH_3)_4]^{2+} + 2OH^- \tag{7}$$

These $[Zn(NH_3)_4]^{2+}$ complexes stock free Zn^{2+} ions temporarily and then release them into solution through decomposition, when the free Zn^{2+} ions in the solution become exhausted. This leads to the maintenance of a stable concentration of Zn^{2+} ions and a low level of supersaturation in the system, which inhibits the homogeneous formation of ZnO and facilitates the heterogeneous growth of ZnO branches onto the seeded preformed ZnO nanowire arrays.

2.3.2 Effect of PEI Concentration on the ZnO Branch Growth

PEI is a common capping agent used in hydrothermal ZnO synthesis. It fosters the axial growth and blocks lateral growth of ZnO nanowires by selectively absorbing onto the side surfaces. Similar to ammonia, PEI also provides OH^- ions and raises pH value. More importantly, it can also promote the solubility of zinc ions in the nutrient precursor by complexing with free Zn^{2+} ions and depressing the opportunities of free Zn^{2+} ions to combine with OH^- ions to form precipitate.[23, 28] During the inspection of the effect of PEI concentration on the growth of ZnO nanoforests, a fascinating phenomenon was easily noticed (Figure 4). Without adding PEI and ammonia, the trunks of ZnO nanotrees are all flat-top surrounded by compact ~650 nm-long branches (Figure 2H). After adding 0.0035 M of PEI into the synthesis solution, the branches grown on the preformed ZnO nanowire arrays were slim and sparse. When the PEI concentration was increased to 0.005 M, the branches became ~250 nm long and further sparse. The trunks' top surface was converted into a pencil-like shape. At 0.007 M of PEI, sharper ZnO nanowire arrays barely with branches were produced, suggesting either no branches could grow or growing branches were eroded off right away. In our study, the highest PEI concentration used was 0.007 M, because neither ZnO branches were grown on the preformed ZnO nanowire arrays nor precipitation was formed in the solution when higher PEI concentration was introduced.

The reason for the phenomena observed in Figure 4 is because PEI can trigger surface dissolution of both preformed ZnO trunks and forming ZnO branches. As previously reported, OH^- ions attracted by the polar top planes can boost the growth and also erode the top surfaces of ZnO, depending on the amount of OH^- ions.[37] When the amount of OH^- ions in the precursor solution was high enough after adding PEI, the ZnO erosion reaction (8) dominates over the ZnO precipitation reactions (3) and (4).

$$ZnO + 2OH^- \rightleftharpoons ZnO_2^{2-} + H_2O \tag{8}$$

The dissolution process started from the nonpolar facets and the edge of polar surfaces of the preformed hexagonal ZnO nanowires. Therefore, the trunk of the preformed ZnO nanowires were carved into sharp pencil-like shape, and the forming branches were worn away. Compared to that of the preformed ZnO nanowire arrays (Figure S2C), the surface of the nanowires' trunk became rather rough after trying to grow ZnO nanobranches with *c*(PEI) = 0.007 M (Figure 4HP3) due to the erosion by extra OH^- ions. The final shape of these ZnO nanotrees reflects the balance of ZnO surface nucleation and chemical corrosion (reactions 3+4 *vs* 6). Other than modulate the growth process of ZnO nanowires/branches, PEI can sculpture preformed ZnO nanowires into slim and sharp shape.

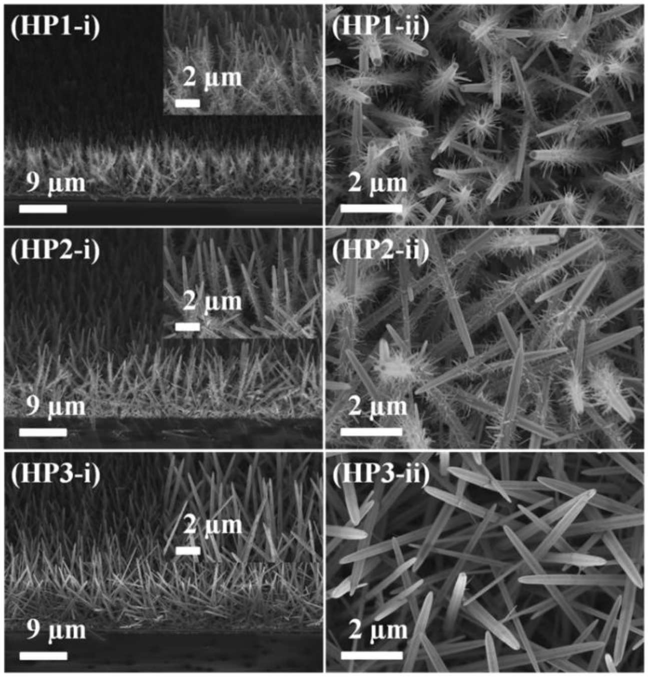

Figure 2.4 SEM images of the obtained ZnO nanoforests after growing ZnO nanobranches onto the preformed ZnO nanowire arrays in precursor solutions with no ammonia but different concentrations of PEI. HP1: c(PEI) = 0.0035 M; HP2: c(PEI) = 0.005 M; and HP3: c(PEI) = 0.007 M.

XRD patterns of ZnO nanoforests with increasing PEI concentration are present in Figure 5A. It can be also clearly seen that all the peaks belong to hexagonal wurtzite ZnO (JCPDS Card No. 36-1451) without any secondary peaks. The relative intensity of the $(10\bar{1}0)$, $(10\bar{1}1)$, $(10\bar{1}2)$, $(11\bar{2}0)$, $(10\bar{1}3)$, $(11\bar{2}2)$, and $(20\bar{2}1)$ peaks did not fluctuate following the same way as the branch length variation. From sample H to HP1, erosion of side branches engendered fortifying $T_c(0002)$ and dwindling $T_c(10\bar{1}0)$ and $T_c(10\bar{1}1)$. From sample HP2 and HP3, $T_c(10\bar{1}0)$ and $T_c(10\bar{1}1)$ were oddly heightened with continuously trimmed branches, while $T_c(0002)$ descended. The diffraction on 0002 was debilitated because the extra PEI and OH^- ions corroded both ZnO trunk nanowires and secondary branches short. Both $(10\bar{1}0)$ and $(10\bar{1}1)$ crystal surfaces were exposed after the corrosion by OH^- ions, and the diffraction on these two planes were strengthened, hence $T_c(10\bar{1}0)$ and $T_c(10\bar{1}1)$ were both boosted for HP2. More disclosed $(10\bar{1}0)$ plane surface was observed from sample HP3, so slimmer ZnO nanowires and higher $T_c(10\bar{1}0)$ were observed. Meanwhile, the slightly depressed $T_c(10\bar{1}1)$ suggests the corrosion of the $(10\bar{1}1)$ surface was slowed down.

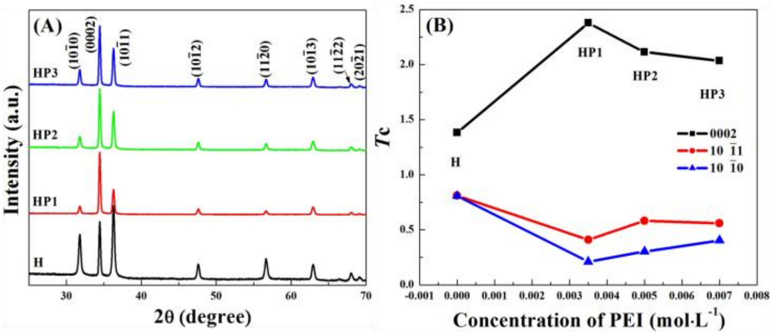

Figure 2.5 (A) XRD patterns of samples H, HP1, HP2 and HP3. (B) Variations of the calculated Harris's texture coefficient, T_c, for 0002, $10\bar{1}0$, and $10\bar{1}1$ diffractions based on the XRD patterns in (A).

2.3.3 Synergistic Effect of Ammonia and PEI Concentrations on the ZnO Secondary Branch

Although ammonia and PEI share similar characteristics, such as raising OH^- ion concentration and coordinating with Zn^{2+} ions to increase zinc solubility, their individual effects on the ZnO secondary branch growth onto the preformed nanowire arrays are quite different as discussed above. To probe their synergistic influence on the ZnO nanobranch growth onto the preformed nanowire arrays to form nanoforests, the concentration of PEI were respectively adopted at 0.0035 M, 0.005 M and 0.007 M under fixed ammonia concentration of 0.15 M since the ZnO branches grew pretty long with 0.15 M ammonia and no PEI (Figure 2HA5). As shown in Figure 5, all the ZnO branches of sample HAP1 became sharp-ended and sparsely dispersed, after adding 0.0035 M PEI into the nutrient solution with 0.15 M of ammonia. When the PEI concentration was increased to 0.005 M, the sharp-ended branches were extended from ~180 nm to ~400 nm (Figure 6HAP2). With 0.15 M of ammonia and 0.007 M of PEI in the nutrient solution system, plenty of well-dispersed nanofiber-like branches were nearly perpendicularly orientated and randomly aligned along individual 6-fold planes of the preformed ZnO nanowire trunks, with aspect ratio of ~600 (~12 µm in length and ~20 nm in diameter, Figure 6HAP3). This is surprisingly different from the results obtained without adding ammonia, which formed hardly branches (Figure 4HP3). These willow-like nanotree arrays construct a highly inter-connected 3D nano-matrix, and are expected to have robust electric conductivity and mechanical stability, endowing broad application potentials.[45, 48-49]

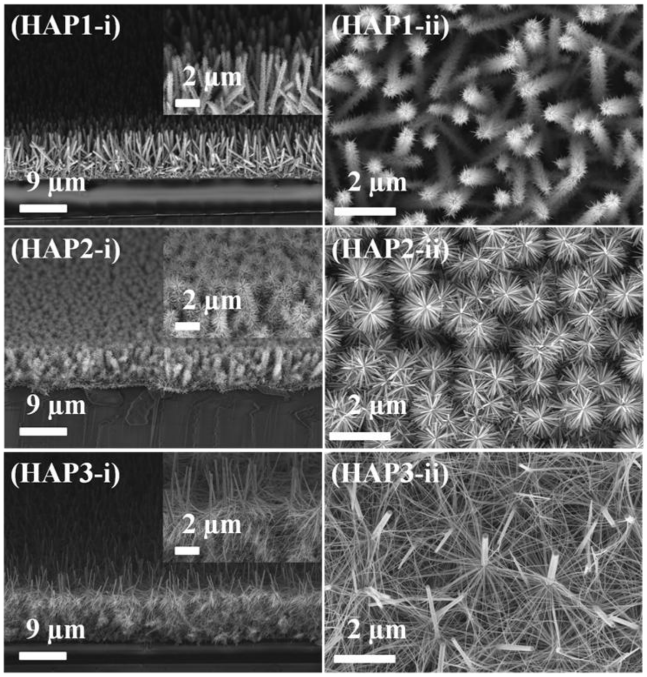

Figure 2.6 SEM images of ZnO nanoforest after growing ZnO nanobranches onto the preformed ZnO nanowire arrays from the precursor solution with 0.15 M of ammonia and varying

concentrations of PEI. HAP1: *c*(PEI) = 0.0035 M; HAP2: *c*(PEI) = 0.005 M; HAP3: *c*(PEI) = 0.007 M.

XRD patterns of samples HA5, HAP1, HAP2 and HAP3 in Figure 6A demonstrated that not only all these samples are pure ZnO without other phases, but also the fluctuations of the relative $(10\bar{1}0)$, $(10\bar{1}1)$, $(10\bar{1}2)$, $(11\bar{2}0)$, $(10\bar{1}3)$, $(11\bar{2}2)$, and $(20\bar{2}1)$ peak intensities are tightly associated with the branches evolution to form the nanoforests as shown in Figure 6. Reciprocally supported by these SEM images, XRD patterns and the calculated Harris's texture coefficient in Figure 7 both demonstrated that sample HAP1 with shorter secondary branches has more intense orientation on 0002 diffraction. For HAP2 and HAP3, the branches were substantially stretched and prolonged, hence the lateral $10\bar{1}0$ and $10\bar{1}1$ diffractions were fortified, inducing $T_c(10\bar{1}0)$ and $T_c(10\bar{1}1)$ climbing up, while the 0002 diffraction decreased relatively with lowering $T_c(0002)$.

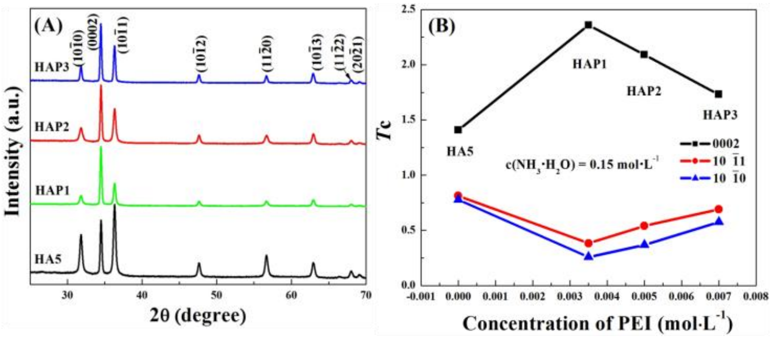

Figure 2.7 (A) XRD patterns of samples HA5, HAP1, HAP2 and HAP3. (B) Variations of the calculated Harris's texture coefficient T_c for 0002, $10\bar{1}0$ and $10\bar{1}1$ diffractions based on the XRD patterns shown in (A).

The morphology and crystal structure of the as-synthesized ZnO nanoforests were also studied by TEM and HRTEM. Figures 8A and 8B exhibit representative SEM and TEM images of an individual ZnO nanotree from sample HA5, respectively. Secondary branches were densely and randomly aligned on the preformed ZnO trunks. The secondary nanobranches have a diameter of ~40 nm. Figure 8C shows a SAED pattern taken from the whole nanotree shown in Figure 8B. No significant indication of orientation preference of the secondary branches was observed. Figure 8D shows a typical HRTEM image of the tip of such a secondary branch and the corresponding SAED pattern (inset). HRTEM studies and electron diffraction analysis show that all ZnO secondary branches have a single-crystal hexagonal structure with the [0001] direction parallel to their long-axis direction. Figures 8E and 8F are SEM and TEM images of a typical individual willow-like nanotree of sample HAP3. Densely-stacked slim nanofiber-like branches are shown upwardly orientated, well dispersed and distributed along their preformed ZnO trunk. In Figure 8F, some branches were broken off the trunk during the ultrasonication of TEM sample preparation. Figure 8G shows a SAED pattern taken from the entire willow-like nanotree in Figure 8F exhibiting randomly oriented secondary branches, *i.e.*, all the branches do not possess the same crystallographic orientation and alignment. Figure 8H shows a typical HRTEM image and the corresponding SAED pattern (inset) of a secondary branch from a willow-like nanotree presenting a single-crystal hexagonal structure with the [0001] direction parallel to its long-axis direction.

After assembling all the typical SEM images of various ZnO nanotrees shown in Figures 2, 6 and 6 into Figure 1, the effluence of the PEI and ammonia concentrations on adjusting the morphology of ZnO nanotrees is quite evident. Low concentration ammonia eroded the branches on ZnO nanotrees into petal-like structure, attributed to the competing mechanisms by producing homogeneous nuclei in solution and heterogeneous growth on the trunks after adding low amount of ammonia into the solution system. When its amount was sufficient high, ammonia coordinated with Zn^{2+} ions, assisting nucleation and growth of ZnO branches and also inhibiting the formation of homogeneous nuclei. On the other hand, PEI etched the nonpolar surfaces of ZnO nanowires, but still supported the growth on polar surfaces along *c*-axis. Surprisingly the cooperation of ammonia and PEI stretches and extends the growth of ZnO secondary branches onto the nanowire arrays substantially long and slim, forming an intersecting 3D network. Therefore, based on the interesting results discussed above, we believe that desirable architectures of 3D ZnO nanoforests can be readily designed and programmed via tailoring and engineering ammonia and PEI concentrations in nutrient solutions with aims to control their functional properties and fulfill the demands from various potential applications, for example, photoelectrochemical water splitting discussed below, in addition to energy storage and conversion.

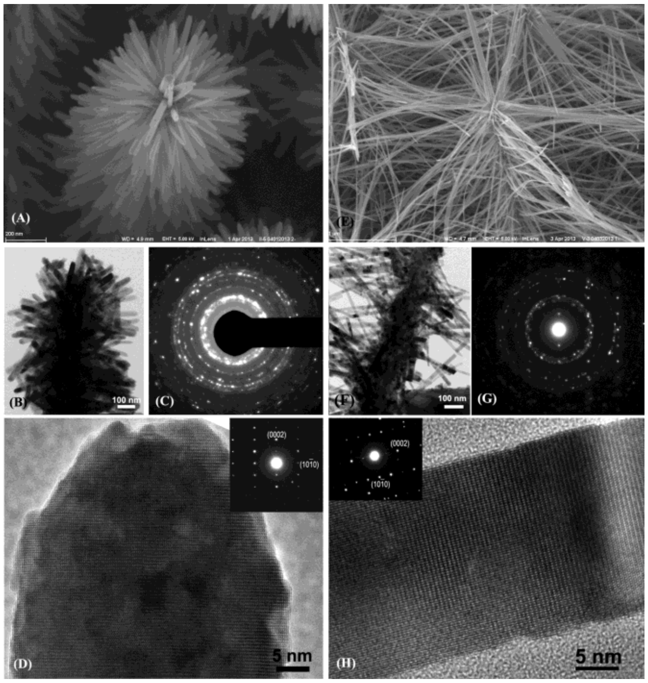

Figure 2.8 (A) SEM, (B) TEM image and (C) SAED pattern of an individual ZnO nanotree of sample HA5. (D) HRTEM image and SAED (inset) of a branch from the ZnO nanotree shown in (A-C). (E) SEM, (F) TEM image and (G) SAED pattern of a willow-like ZnO nanotree of

sample HAP3. (H) HRTEM image and SAED pattern of a branch from the willow-like ZnO nanotree shown in (E-G).

2.3.4 Photoelectrochemical Water Splitting Performance of the ZnO Nanoforests

Tree-like ZnO nanowire anodes with maximized dense nanobranches have been foreseen to exhibit optimal solar cell performance, due to the nanobranches filling the space between the nanowire trunk substantially increase the surface area and act as single-crystalline charge transport pathways with shorter distance.[50] It has demonstrated that long branched tree-like ZnO nanowire dye-sensitized solar cells (DSSCs) can raise the overall light-conversion efficiency almost 5 times compared with DSSCs constructed by upstanding ZnO nanowires. It was attributed to enlarged surface area for higher dye loading and light capture, and reduced charge recombination by providing direct conduction pathways along the crystalline ZnO nanotree multi-generation branches.[11] Moreover, our group recently demonstrated that 3D ZnO@MnO_2 core@shell nanoforest electrodes for electrochemical energy storage devices offer 5 times higher areal capacitances, advanced rate capability, and better charge-discharge stability, compared with their corresponding nanowire array counterpart. Although branched ZnO nanotetrapods as photoanodes have been employed in PEC water splitting, ZnO nanoforests have not been utilized to build a 3D interconnected conductive matrix for solar-to-hydrogen production yet.[45] To fill the gap and unearth more potentials of ZnO nanoforests in energy storage and conversion, three typical architectures, i.e. ZnO nanowire arrays, brush-like nanoforest (sample HA5) and willow-like nanoforest (sample HAP3), were evaluated as photoanodes (within the same footprint of 0.7 cm^2) in PEC cells for hydrogen generation from water splitting, respectively (Figure 9).

Figure 9A shows the linear sweep voltammograms recorded from -0.5 to +1.2 V (vs. Ag/AgCl) on the three typical ZnO nanoarchitectures under irradiation (100 mW/cm^2) as well as the nanowire arrays in the dark for comparison. The scan for the nanowire arrays in the dark displayed a negligible current density in the range of ~0.001 mA/cm^2. Illuminated by the simulated solar light, the willow-like ZnO nanoforest stood out with its maximum current density of 0.919 mA/cm^2 at +1.2 V (vs. Ag/AgCl), which is more than 267% and 126% advancement in comparison with the ZnO nanowire arrays (0.344 mA/cm^2) and brush-like nanoforest (0.727 mA/cm^2). Significantly, no saturation of photocurrent density was observed on these three samples at the highest measured potential (i.e. +1.2 V (vs. Ag/AgCl) in this study), suggesting efficient charge separation and collection in those architectures under solar irradiation. More impressively, this maximum current density achieved from our willow-like ZnO nanoforest (0.919 mA/cm^2 at +1.2 V vs. Ag/AgCl) demonstrates enhancements of 765%, 644%, and 367% compared with the values recently reported from branched ZnO nanotetrapods (0.12 mA/cm^2 at +0.31 V vs. Ag/AgCl),[45] ZnO thin film (0.1425 mA/cm^2 at +1.0 V vs. Ag/AgCl),[51] and ZnO nanocorals (0.25 mA/cm^2 at +1.2 V vs. RHE), respectively.[52]

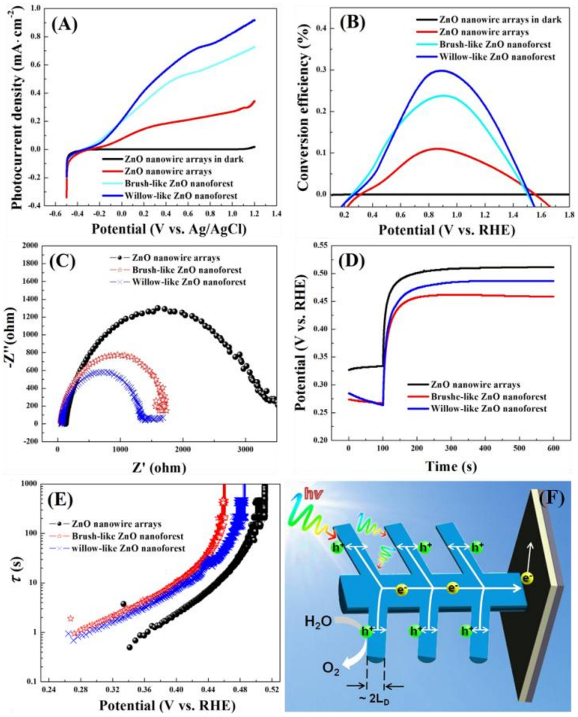

Figure 2.9 (A) Photocurrent density-potential curves; (B) photoconversion efficiency; (C) impedance spectra; (D) response of V_{oc}; and (E) photoelectron lifetime from three nanostructured ZnO architectures: nanowire arrays, short-branched nanoforest, and willow-like nanoforest. (F) Schematic model displaying the illuminated photoanode to explain the enhanced charge transport and light trapping in willow-like ZnO nanoforest.

To quantitatively evaluate the efficiency of PEC hydrogen generation from different ZnO nanostructures, the photoconversion efficiency (PCE) is calculated based on the following equation:[53]

$$\mathrm{PCE} = \frac{J_{\mathrm{p}}}{P_0}\left(E_{\mathrm{rev}}^{0} - |E_{\mathrm{b}}|\right) \tag{9}$$

where J_{p} is the photocurrent density (mA·cm^{-2}); P_0 is the incident light intensity (100 mW·cm^{-2}); $E_{\mathrm{rev}}{}^{0}$ is the standard state-reversible potential for water splitting (1.23 eV); and E_{b} is the applied bias potential, which is the difference between the potential at the measuring point and the electrode open-circuit potential under the same illumination intensity. As shown in Figure 9B, the ZnO nanowire arrays achieved its highest efficiency of 0.110% at 0.85 V (vs. RHE), consistent with the previously reported typical value for undoped ZnO nanowire arrays.[54] The conversion efficiency for the brush-like nanoforest reached 0.236% at 0.85 V (vs. RHE). As a champion in all homogeneous nanostructured ZnO photoanodes reported here, the willow-like nanoforest distinguished itself with photoconversion efficiency of 0.299% at 0.89 V (vs. RHE) from other pure ZnO nanostructures with neither doping nor noble metal decoration, such as branched ZnO nanotetropods (0.045% at +0.82 V vs. RHE) and 3D ZnO nanosuperstructures (0.028% at +0.98 V vs. RHE).[45, 55]

To certify that longer branches can facilitate charge migration, electrochemical impedance spectroscopy (EIS) was measured for these three typical ZnO nanoarchitectures over the frequency range of 10^{-2} -10^{6} Hz. The Nyquist plots (Figure 9C) consist of one dominant semicircle, whose diameter is associated to charge transfer resistance at ZnO/electrolyte interface.[21, 56] With prolonging branches, the ZnO nanoforests exhibited contracting diameters comparing with the nanowire array counterpart, implying that branching of the nanowire arrays motivated better charge transfer. With the longer and thinner ZnO branches, the willow-like nanoforest takes full advantage of space by filling the voids, and so offering minimized charge transfer resistance.

Photoelectron lifetime is associated with decay rate V_{oc} by the following equation:[21, 57]

$$\tau = \frac{k_{\mathrm{B}}T}{e}\left(\frac{\mathrm{d}V_{\mathrm{oc}}}{\mathrm{d}t}\right)^{-1} \tag{10}$$

where τ is the photoelectron lifetime, k_{B} is Boltzmann's constant, T is the temperature, e is the charge of a single electron, and V_{oc} is the open-circuit voltage. With the morphology transited from the ZnO nanowire arrays to nanoforests, the photoelectron lifetime was evidently prolonged (Figures 9D and 9E), implying less charge trapping and more efficient charge separation. However, compared with that of the brush-like nanoforest, the photoelectron lifetime of the willow-like nanoforest was slightly reduced. Two possible reasons were hypothesized. The first one is because the larger surface area of the willow-like nanoforests yields more photoelectron and hole pairs. Subsequently the opportunity of recombination increases and the average lifetime of photoelectrons is lightly decoupled. At the meantime, fiber-like branches of willow-like nanoforest reached far enough from one trunk to another to connect each other. However, their junctions are potential active spots where several photo-generated electrons and holes can recombine.[58] Even with this small drawback, the willow-like ZnO nanoforest is still not hindered from possessing overall “champion” PEC water splitting performance.

In the domain of homogeneous ZnO nanostructures as electrode material for PEC hydrogen generation, such unbeatable performances of willow-like nanoforests can be interpreted from the following aspects. First of all, the pronouncedly amplified surface area and roughness factors of nanoforests engendered huge photocurrent density increase, associated with augmented light and photon harvesting. Like nature trees, upstanding nanotree arrays provided straight-forward light path and long penetration depth of light, avoiding the thickness limitations of densely stacked nanoparticles. The nanosized branches effectively help extend the light propagation path and improve light trapping, because of the multiple times of internal light refection and scattering on the surface of branches.[43, 59-60] As a complicated 3D maze for light, nanoforest configuration entirely quadrupled the opportunities of light-ZnO interactions (Figure S6). It was reported that tree-like ZnO micro/nanostructures have broader absorption in solar spectrum than ZnO nanowires, because tree-like shapes can activate maximized excitonic band gaps of wurtzite ZnO.[61] Thus, resulting from amplified surface area and superior light-trapping capability, the charge generation efficiency was greatly improved.

To elucidate the superiority of our ZnO nanoforest photoanodes, the mechanism of charge transport have also been carefully considered. As illustrated in Figure 9F, under irradiation, photo-generated electron and hole pairs on the ZnO photoanode decompose water (H_2O) molecules into gaseous oxygen (O_2), hydrogen ions (H^+), and electrons at the ZnO/electrolyte interface. Gaseous O_2 molecules are created at the anode and H^+ ions migrate to the cathode through electrolyte. Meanwhile, the photoelectrons flow to the cathode through external circuit and reduce H^+ ions into gaseous hydrogen (H_2). The efficiency of photoanode predominantly relies on slowing down the electron-hole recombination and improving charge transport properties in the electrolyte/photoanode/back electrode configuration.[62] Our ZnO nanoforests have immeasurable ultrathin branches, especially the fiber-like branches of the willow-like nanoforest with diameter of ~20 nm (Figure 5HAP3 and Figure 7D-H), which efficiently shrink the diffusion length (L_D) of holes and prevent carrier recombination.[38] The willow-like nanoforest with the lowest charge transfer resistance was ascertained by EIS data in Figure 2.9C. In addition, the well crystallized ZnO branches and trunks facilitated electron transportation as conductive and directional highway, especially along their *c*-axis, several orders of magnitude faster than those densely packed nanoparticles.[49] All those factors expedite the charge separation, the transportation of holes to the ZnO/electrolyte interface for water oxidation, and the delivery of photoelectrons to the current collector on the back, minimize of recombination probabilities of photocarriers and optimize charge transfer kinetics.

The third consideration is charge collection efficiency, which is associated with the interfacial surface area and the connection between the ZnO nanoforest photoanode and ITO substrate. The large surface area of the ZnO nanoforest induce a full contact and a rapid delivery of holes from reaction sites to water, facilitating the hole transfer kinetics at ZnO/electrolyte interface and boosting collection efficiency of holes. Moreover, like nature trees delivering water and carbohydrates, our dendritic ZnO nanotrees optimize efficient photoelectron collection from myriad terminals to the central trunks, which are tightly rooted on the current collector. Hence, the peculiar geometry of our ZnO nanoforests provides highly augmented surface area without sacrificing electron transportation and collection, and ensures efficient charge collection efficiency.

This work manipulated the principle of morphological modulation for 3D ZnO nanoforests by tuning the concentrations of ammonia and PEI (therefore, their relative ratio). A nano-superstructure, specifically willow-like ZnO nanoforest, can surprisingly harvest solar light and deliver fabulous PEC water splitting performance. According to above analysis, the special geometry of our ZnO nanoforests guarantees high efficiency in charge generation, transportation, and collection processes. Therefore our ZnO nanoforest outperforms in all homogeneous ZnO photoanodes for hydrogen generation via PEC water splitting. This superstructure is also highly expected to outperform other morphologies in various energy storage and conversion devices, such as batteries and solar cells. On the other side, an Achilles' heel of the pure ZnO nanoforest is that they are still not able to capture visible light in the solar spectrum, restricted by inherently large band gap of ZnO.[63-64] It is believed that this drawback can be tackled by substitutional doping, decorating with noble metal, sensitizing and integrating into core/shell heterogeneous nanostructures.[53, 63-69] Therefore, the as-prepared ZnO nanoforest reported here are qualified to be an ideal photo-active base material.[63]

2.4 Conclusion

In summary, we have successfully fabricated various distinctive 3D ZnO nanoforests via a facile hydrothermal synthesis of ZnO nanobranches onto preformed nanowire arrays. The morphology of the 3D ZnO nanotrees was tailored by tuning the PEI and ammonia concentrations, which mediate the surface chemistry and shape the directional growth of the ZnO crystalline nanobranches. The individual function and synergistic influence of PEI and ammonia on the growth of the ZnO nanobranches onto the preformed ZnO nanowire arrays were symmetrically studied. The incredible architecture characteristics endowed the willow-like ZnO nanoforest miraculous PEC water splitting performance, including small charge transfer resistance, long photoelectron lifetime, paramount photocurrent density (0.919 mA/cm^2 at +1.2 V, vs. Ag/AgCl), and more importantly “champion” photoconversion efficiency (0.299% at 0.89 V, vs. RHE), which leads the realm of homogeneous ZnO nanostructures. Therefore, this work opens up an unprecedented avenue by governing desirable 3D ZnO nanostructures based on demands, and broadens the application potentials of 3D nanotechnology to both minimized functional and large-scale industry devices. Moreover, it is expected that these 3D ZnO nanoforests will make surprising innovations in the field of PEC hydrogen production in conjunction with doping and decoration, and greatly benefit the entire energy storage and conversion field.

CHAPTER III

ZNO@MNO2 NANOFORESTS FOR ENERGY STORAGE

3.1 Introduction

Supercapacitors and lithium ion batteries (LIBs) have attracted increasing attention in recent years as energy storage devices, owing to the high power density, excellent reversibility, long cycle life and good operational safety of the former and the high energy density of the latter.[4, 70-71] However, their miniaturization has not kept pace with advances of microelectromechanical systems (MEMS), biomedical and autonomous devices, whose desired on-board power storage happens on exceptionally small geometric scales. In either unit weight (Wh kg^{-1}) or volume (Wh L^{-1}), the amount of energy stored on a given footprint (J mm^{-2}) of these devices is desirable to surpass that of conventional two-dimensional (2-D) battery and supercapacitor configurations. To overcome the shortcomings of these technologies while developing more powerful energy storage devices,[3] one major approach pursued very recently is based on the fabrication of 3-D electrode structures at the nanoscale.

Compared with compact 2-D counterparts, 3-D architectures take advantage of the vertical dimension-height. 3-D nanostructured electrodes possess higher surface/body ratios, larger surface areas, more surface active sites within a small footprint area, and accordingly enlarged areal capacity.[72-73] Therefore, their synthesis is now considered as a new strategy for powering MEMS and other small autonomous devices. Some efforts have been devoted to engineering 3-Dnanostructures as energy storage electrodes.[13-14, 74-75] For example, Liu *et al.* built electrodes of Co_3O_4@MnO_2 nanowire arrays using sacrificial reactive 3-D carbon template layers. Xia *et al* synthesized Co_3O_4@NiO core@shell nanowire arrays for supercapacitors with high capacitance and good cycling stability. Yan *et al.*coated V_2O_5 on SnO_2 nanowire arrays to bridge the performance gap between batteries and supercapacitors for high-rate LIBs. All these 3-D core@shell heterostructures consist of high conductive one-dimensional (1-D) nanowires as the core and electroactive transition metal oxide or hydroxide as shells and branches.

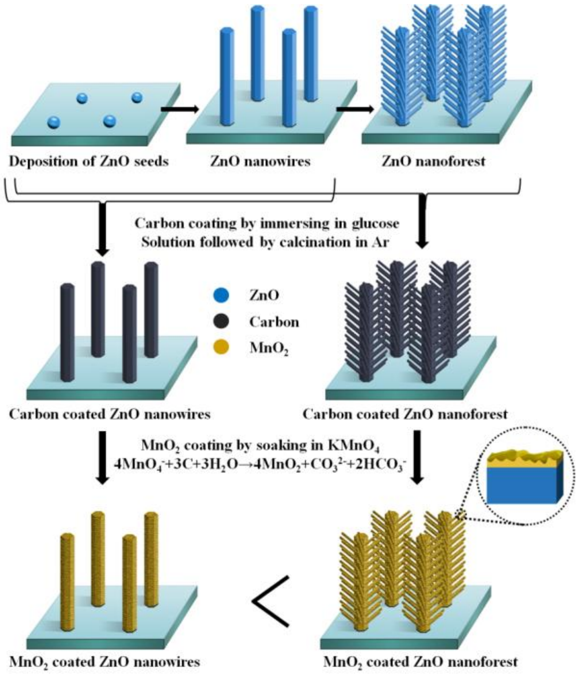
Deposition of ZnO seeds
ZnO nanowires
ZnO nanoforest
Carbon coating by immersing in glucose
Solution followed by calcination in Ar
ZnO
Carbon
MnO$_2$
Carbon coated ZnO nanowires
Carbon coated ZnO nanoforest
MnO$_2$ coating by soaking in KMnO$_4$
$4MnO_4^- + 3C + 3H_2O \rightarrow 4MnO_2 + CO_3^{2-} + 2HCO_3^-$
<
MnO$_2$ coated ZnO nanowires
MnO$_2$ coated ZnO nanoforest

Figure 3.1 Schematic illustration of the fabrication process for the designed 3-D ZnO@MnO_2 core@shell nanowire array electrode and its nanoforest counterpart. The latter possesses further boosted electrochemical performance than the former.

In this work, we designed a novel architecture composed of branched nanowire arrays, *i.e.* forest of nanotrees, to further boost electrochemical performance over 1-D nanowire arrays, inspired by branched trees with larger surface area to capture more sunlight.[11] Specifically, we first fabricated both 3-D ZnO@MnO_2 core@shell nanowire arrays and branched nanowire array counterpart, *i.e.* nanoforest, using hydrothermal and redox processes. The whole fabrication process is schematically illustrated in Figure 4.1. Moreover, our electrochemical characterization revealed that the 3-D ZnO@MnO_2 core@shell nanoforest electrodes possess higher capacitance (5 times), better rate performance, and longer retention of capacitance at higher current densities, compared to their nanowire array counterparts.

To the best of our knowledge, no electrodes composed of nanoforests have been applied to electrochemical energy storage devices yet. This new design not only fills the void in the gallery of heterostructured nanomaterials with a 3-D skeleton applied in electrochemical energy storage devices, but also provides a direction to meet the miniaturization requirements of powering MEMS and other miniaturized functional devices.

3.2 Experimental

3.2.1 Materials

Sodium hydroxide (NaOH), zinc acetate [$Zn(O_2CCH_3)_2 \cdot 2H_2O$], hexamethylenetetramine ($C_6H_{12}N_4$, HMTA), polyethylenimine (PEI), ammonia ($NH_3 \cdot H_2O$) and glucose ($C_6H_{12}O_6$) were purchased from Sigma-Aldrich. Zinc nitrate hydrate [$Zn(NO_3)_2 \cdot 6H_2O$] and potassium permanganate ($KMnO_4$) were purchased from Alfa Aesar. All reagents were of analytical grade and were used without further purification.

3.2.2 Preparation of 3-D ZnO@MnO$_2$ Core@shell Nanostructures

To demonstrate the advantages of nanoforests over corresponding nanowire arrays in electrochemical energy storage, two different 3-D nanostructures, *i.e.* ZnO@MnO$_2$ nanowire arrays and ZnO@MnO$_2$ nanoforests, were synthesized and compared. The fabrication procedures are illustrated in Figure 4.1. In the first step, ZnO nanoparticles seed solution was obtained through adding 25 mL of 0.03 M sodium hydroxide (NaOH) ethanol solution into 37.5 mL of 0.01 M zinc acetate [$Zn(O_2CCH_3)_2 \cdot 2H_2O$] ethanol solution drop by drop, and then the mixture was actively stirred at 60 ℃ for 2 h. The seed solution was drop casted onto a titanium substrate. ZnO nanowire arrays were grown from these ZnO quantum dot seeds through immersing in an aqueous precursor solution containing 0.025 M zinc nitrate hydrate [$Zn(NO_3)_2 \cdot 6H_2O$], 0.025 M hexamethylenetetramine ($C_6H_{12}N_4$, HMTA), 0.1 M polyethylenimine (PEI), and 0.15 M ammonia ($NH_3 \cdot H_2O$) at 60-90 ℃ for 7-15 h. Then the grown ZnO nanowire arrays were thoroughly rinsed with deionized water, and dried in air. After annealed at 350 ℃ in air for 10 min to remove residual organics, ZnO nanowire arrays on Ti substrate were obtained. ZnO nanoforests were obtained through adding ZnO seed solution onto the as-prepared ZnO nanowire arrays as the backbone and subsequently conducting a similar hydrothermal reaction as described above except without adding ammonia or PEI to grow ZnO nano-branches onto the ZnO nanowire array backbones.

To fabricate the final ZnO@MnO$_2$ nanowire arrays and ZnO@MnO$_2$ nanoforests, ZnO@C nanowire arrays and nanoforests were obtained through immersing ZnO nanowire arrays and nanoforests into glucose aqueous solution (0.03 M), respectively, for 1 h and then annealed in argon atmosphere at 500 ℃ for 3 h. This annealing step carbonizes the glucose molecules absorbed onto the surface of ZnO nanowire arrays and nanoforests. Subsequently, electroactive MnO_2 nanoparticle coatings were purposely decorated onto ZnO nanowire arrays and nanoforests through immersing the hybrid ZnO@C nanowire arrays and nanoforests in 0.03 M $KMnO_4$ aqueous solution for 1 h at room temperature, respectively. A thin layer of MnO_2 nanoparticles was grown on the 3-D ZnO nanostructures through the redox reaction between the carbon coating on ZnO with the $KMnO_4$ solution. At last, the MnO_2 nanoparticles coated ZnO nanowire arrays and nanoforests were rinsed with deionized water and dried at 80 ℃ overnight in vacuum.

3.2.3 Characterization

The morphology and crystal structure of the ZnO@MnO_2 nanowire arrays and nanoforests were characterized through scanning electron microscopy (Carl Zeiss Sigma VP Field-Emission SEM at 2-5 kV), transmission electron microscopy (JEOL JEM-2010 UHR TEM) and high-resolution TEM (HRTEM), coupled with selected area electron diffraction (SAED) and energy dispersive X-ray spectroscopy (EDS). The surface chemical composition and oxidation state of the samples were determined by X-ray photoelectron spectroscopy (XPS) measurement (Kratos AXIS 165 X-ray photoelectron spectrometer). Raman spectroscopy was conducted on a Bruker SENTERRA RAMAN microscope with a 785 nm laser as the excitation source.

3.2.4 Electrochemical Measurements

Cyclic voltammetry (CV) measurements were conducted on a Gamry Reference 600 electrochemical workstation, using a three-electrode mode in 1 M Na_2SO_4 aqueous solution with a voltage ranging from -0.2 V to 0.6 V at different scan rates (2 mV s^{-1} to 100 mV s^{-1}). A piece of 0.6 cm^2 sample of ZnO@MnO_2 nanowire arrays or nanoforests on titanium foil was used as the working electrode. The reference electrode and counter electrode were Ag/AgCl and a platinum wire, respectively. With a similar setup, charge/discharge (CD) measurements of ZnO@MnO_2 nanowire arrays or nanoforests as working electrodes were conducted at various current densities of 0.02 to 0.2 mA/cm^2. Electrochemical impedance spectroscopy (EIS) measurements were performed by applying an AC amplitude of 5 mV in a frequency range from 100 kHz to 0.001 Hz.

3.3 Results and Discussion

3.3.1 Morphology and Structure Characterization

Figure 4.2a and b clearly present the 3-D ZnO@MnO_2 core@shell nanowire arrays, and Figure 4.2c and d exhibit the typical morphology of the 3-D ZnO@MnO_2core@shell nanotrees. These arrays have average lengths over 10 μm, grown perpendicularly on the substrate of the titanium current collector (inset of Figure 4.2a). These nanotrees consist of 3-D ZnO@MnO_2 nanowire arrays as the trunks and ZnO@MnO_2 nanorods on the trunks as branches with an average length of ~ 800 nm.

HRTEM images of these ZnO@MnO_2 core@shell nanowire arrays and nanoforests (Figure 4.3) clearly demonstrate that well-dispersed MnO_2 nanoparticlelayers with a thickness of ~ 3 nm were coated on the well-crystalline ZnO nanowire and nanotree backbones, respectively. XPS and Raman data of the as-synthesized 3-D ZnO@MnO_2 nanoforests are not shown here. The peaks located at 1021 eV and 1044 eV are assigned to Zn $2p_{3/2}$ and Zn $2p_{1/2}$, respectively, indicating that the oxidation state of zinc is +2. The peaks at 653.9 eV and 642.3 eV are attributed to Mn $2p_{3/2}$ and Mn $2p_{1/2}$ of MnO_2. The identity of ZnO and MnO_2 from the XPS analysis is consistent with that from the Raman spectrum.

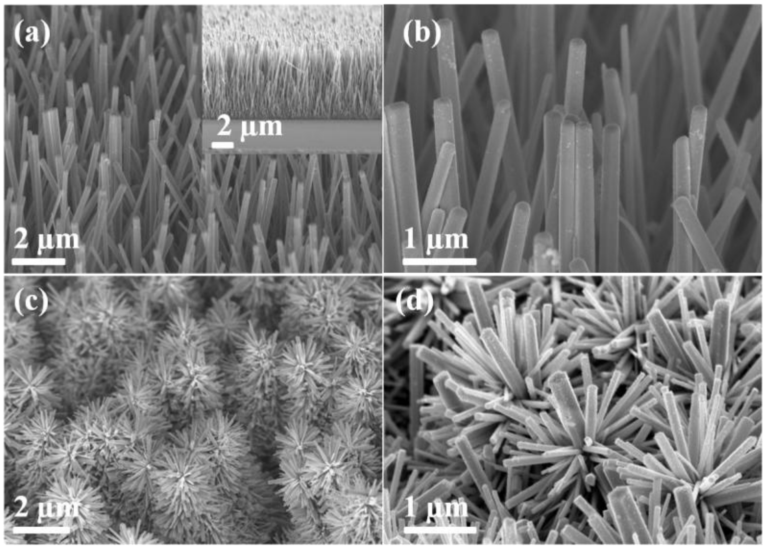

Figure 3.2 Typical SEM images of (A, B) ZnO@MnO_2 nanowire arrays and (C, D) ZnO@MnO_2 nanoforests.

Figures 3.4 a, b and 4.5 show the XPS data taken from the as-synthesized 3D ZnO@MnO_2 core@shell nanoforests. The overview XPS spectrum in Figure 4.5 demonstrates the presence of zinc (Zn 2*p*), manganese (Mn 2*p*), oxygen (O 1*s*) as well as carbon (C 1*s*). The elemental zinc, manganese and oxygen signals are originated from the ZnO core and MnO_2 shell, which is in agreement with the EDS results in Figure 4.6. The carbon peak may come from air exposure during sample preparation or incomplete redox reaction between carbon and $KMnO_4$ during the synthesis. The peaks located at 1021 eV and 1044 eV (Figure 3a) are assigned to Zn $2p_{3/2}$ and Zn $2p_{1/2}$, respectively, indicating the oxidation state of zinc is +2. They are attributed to Mn $2p_{3/2}$ and Mn $2p_{1/2}$ of MnO_2.[12, 13] The identify of ZnO and MnO_2 from these 3D ZnO@MnO_2 core@shell nanoforests was also confirmed by a Raman spectrum as shown in Figure S3.

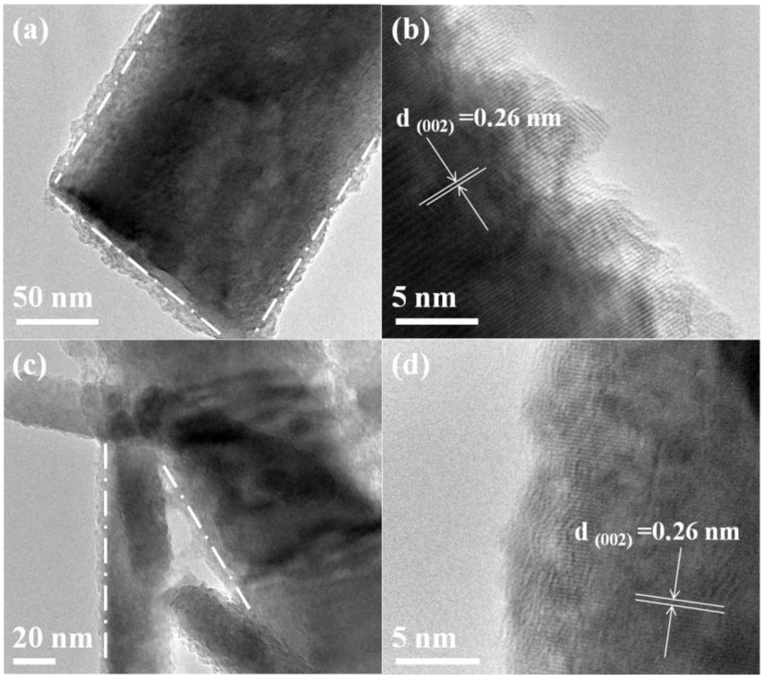
(a)
50 nm
(b)
d (002) =0.26 nm
5 nm
(c)
20 nm
(d)
d (002) =0.26 nm
5 nm

Figure 3.3 Representative TEM and HRTEM images of the synthesized 3-D ZnO@MnO$_2$ core@shell (A and B) nanowire arrays and (C and D) Nanoforests.

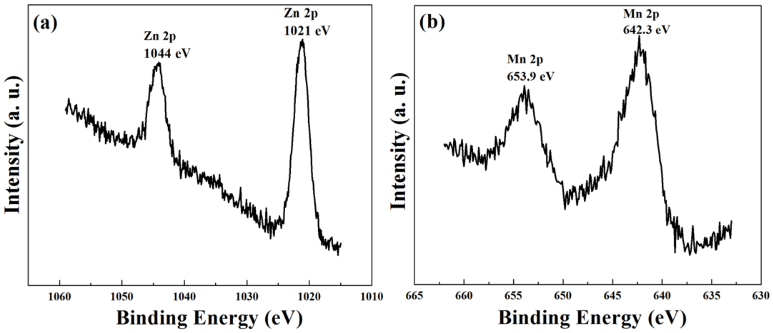

Figure 3.4 Detailed XPS data taken from the synthesized 3D ZnO@MnO$_2$ core@shell nanoforests: (a) the spectrum of Zn 2*p*. (b) the spectrum of Mn 2*p*.

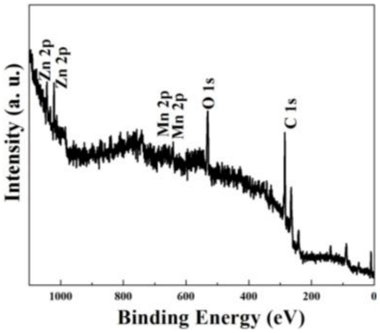

Figure 3.5 Overview XPS spectrum of the as-synthesized 3D ZnO@MnO_2 core@shell nanoforests.

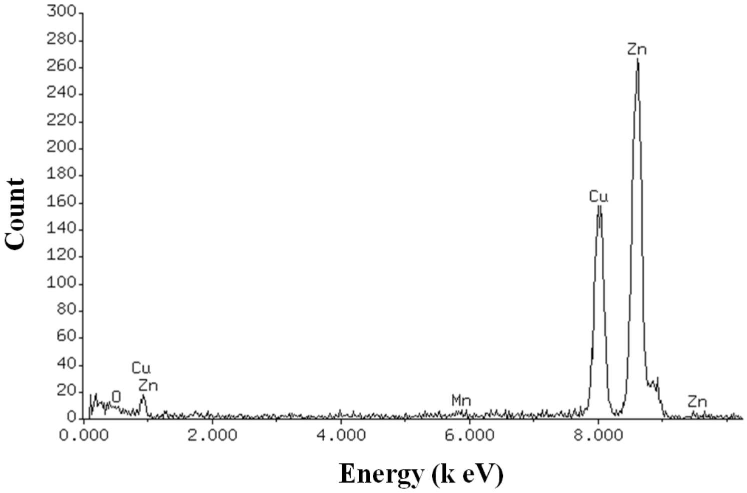

Figure 3.6 Energy-dispersive X-ray spectroscopy (EDS) data taken from the as-synthesized 3D ZnO@MnO_2 core@shell nanoforests shown in Figure 3.3c.

The EDS peaks of zinc, manganese, copper and oxygen are displayed in the spectrum of Figure 3.6. The copper peaks come from the TEM sample grid, and no peaks of other elements are observed. It further confirms that the 3D ZnO@MnO_2 core@shell nanoforests is composed of Zn, Mn, and O, consistent with the XPS results shown in Figures 3.4 and 3.5.

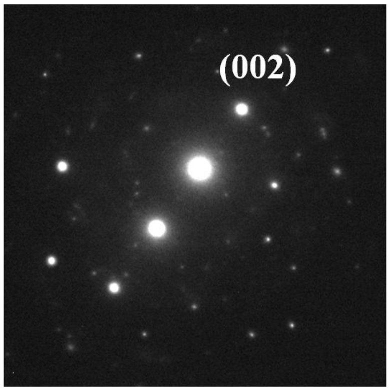

Figure 3.7 SAED patterns of the as-synthesized 3D ZnO@MnO_2 core@shell (a) nanowire arrays and (b) nanoforests.

The SAED pattern in Figure 3.7 can be indexed as hexagonal wurtzite structure of ZnO (JCPDS No. 80-75, *P*63*mc*, $a = b = 0.325$ nm, $c = 0.521$ nm). There is no MnO_2-related diffraction pattern or spot observed in this SAED pattern, which indicates that the MnO_2 coating is amorphous.

3.3.2 Electrochemical Measurements

Cyclic voltammetry (CV) measurements (Figure 4.8a) were performed on the synthesized 3-D ZnO@MnO_2 core@shell nanoforest as working electrodes at different scan rates of 2, 5, 10, 20, 50, and 100 mV s^{-1}. In the potential range of −0.2 to 0.6 V (*vs.* Ag/AgCl), no obvious redox peaks were observed, which is characteristic of electroactive MnO_2 in this range. These CV curves exhibit approximately rectangular shape, especially at slow scan rates. This observation indicates excellent capacitive behaviour and a low contact resistance of the electrodes made from our synthesized 3-D ZnO@MnO_2 core@shell nanoforest, consistent with EIS data discussed below. As commonly observed, the rectangularity gradually expands and is distorted with increasing scan rates. However, the CV curves taken at the same scan rates of electrodes made of the 3-D nanowire array counterpart are evidently more distorted and possess much smaller area (data now shown here). It suggests that the 3-D ZnO@MnO_2 nanowire arrays possess faster downgrading capacitance than the nanoforests even though both nanoarchitectures are composed of the same materials and were fabricated by the same procedure. Furthermore, by comparing the CV curves taken at a scan rate of 2 mV s^{-1} with the same lateral size of electrodes made from the 3-D ZnO@MnO_2 core@shell nanoforest, nanowire array counterpart and pure titanium substrate (Figure 4.8b), a significant increase in integrated CV area was observed for the 3-D ZnO@MnO_2 core@shell nanoforest electrode over the nanowire array electrode, while the pure titanium substrate showed barely any capacitance. The much larger capacitance of the 3-D ZnO@MnO_2 core@shell nanoforest electrode can be attributed to the larger accessible surface area of its unique nanoarchitecture and higher loading of the electroactive MnO_2 nanoparticle coating over that of the 3-D ZnO@MnO_2 nanowire array counterpart at the same footprint.

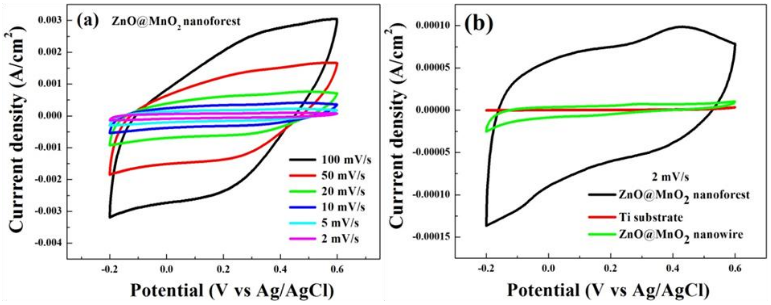

Figure 3.8 (a) Cyclic Voltammetry (CV) curves of ZnO@MnO_2 nanforest electrode at different scan rates. (b) CV curves of the 3-D ZnO@MnO_2 nanoforests, ZnO@MnO_2 nanowire arrays, and titanium substrate as working electrodes at 2 mV s^{-1}.

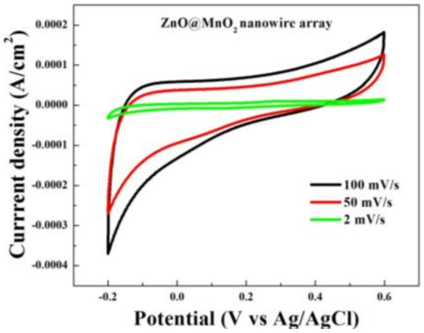

Figure 3.9 Cyclic Voltammetry (CV) curves of the as-synthesized 3D ZnO@MnO_2 nanowire arrays as the working electrode at different scan rates.

From the charge–discharge (CD) measurements conducted on both 3-D ZnO@MnO_2 core@shell nanoforest and nanowire array electrodes (Figure 3.10a, b and c), their specific areal capacitances C_{area} at different current densities (Figure 3.10d) were calculated according to their discharge profiles and the following equation (1):

$$C_{area} = \frac{i * t}{A * Vi} \tag{1}$$

where I is the discharge current, t is the discharge time, A is the effective area of an electrode, and V_i is the voltage interval of the charge-discharge measurements. The capacitance retention was calculated from the ratio of each specific capacitance of different current densities to that of lowest current density (0.02 mA/cm^2).

The respective charging time and discharging time are nearly the same, indicating superior reversibility of charging and discharging reactions of the electrodes made from both the synthesized 3-D ZnO@MnO_2 core@shell nanoarchitectures. The C_{area} of 3-D ZnO@MnO_2 core@shell nanoforest electrode is estimated to be 31.30 mF cm^{-2}, which is nearly 5 times that of the 3-D ZnO@MnO_2 core@shell nanowire array electrode (6.30 mF cm^{-2}). The high C_{area} of the nanoforest electrode results from its enhanced surface area and higher loading amount of MnO_2 nanoparticle coating on the 3-D ZnO nanoforest backbone over those of the nanowire array counterpart. It implies the following electrochemical reactions between MnO_2 and electrolyte with possible intercalation or deintercalation of Na^+ or H_3O^+.

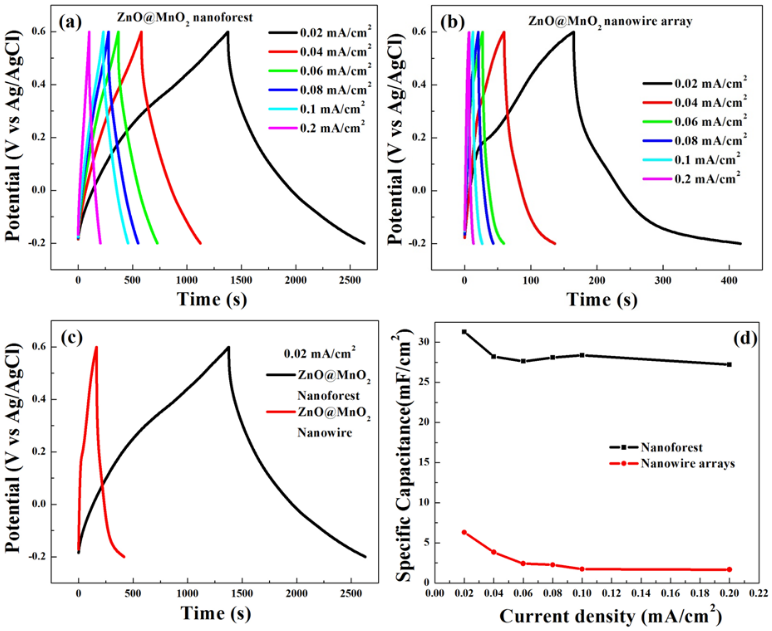

Figure 3.10 (a) Charge/discharge (CD) curves of 3-D $ZnO@MnO_2$ nanoforests as electrode at different current densities; (b) Charge/discharge (CD) curves of $ZnO@MnO_2$ nanowire arrays as electrode at different current densities; (c) CD curves of $ZnO@MnO_2$ nanowire arrays and nanoforests as working electrodes, respectively, at current density of 0.02 mA cm^{-2}; (d) Specific capacitances of $ZnO@MnO_2$ nanoforest and nanowire arrays at different current densities.

$$MnO_2 + M^+ + e^- \leftrightarrow MnOOM,\ M^+ = Na^+ \text{ or } H_3O^+$$

This novel nanoforest architecture utilizes space more efficiently than the nanowire array counterpart, guarantees effective interfacial contact between the electrolyte and the electroactive MnO_2 thin layer, and offers improved electron transfer pathways from the 3-D ZnO nanoforest backbone to the current collector.

Moreover, it is evident that the 3-D $ZnO@MnO_2$ core@shell nanoforest electrode delivers higher capacity than the $ZnO@MnO_2$ core@shell nanowire array electrode. The 3-D $ZnO@MnO_2$ core@shell nanoforest electrode possesses 87% capacitance retention while the nanowire array counterpart has only 26% when discharging current density increases from 0.02 to 0.2 mA cm^{-2}. The higher rate capability of the 3-D $ZnO@MnO_2$core@shell nanoforest electrode may be attributed to the unique 3-D interconnected nanoarchitecture with elevated conductivity from the 3-D ZnO nanoforest backbone and larger specific surface area on the same footprint. These structural advantages promote the maintenance of good electrochemical stability at the larger voltage range and also accelerate charge separation and transport. As reported in the literature, the decrease in specific capacitance with increasing current density results from the internal resistance of electrodes.[76] Therefore, the higher capacitance retention of the 3-D $ZnO@MnO_2$ core@shell nanoforest electrodesuggests a lower internal resistance over the corresponding nanowire array electrode, as confirmed by our EIS data not shown.

Compared to the conventional 2-D electrode configurations of traditional batteries and supercapacitors, and even the most recently engineered 3-D nanostructured electrodes, *e.g.* the as-synthesized 3-D $ZnO@MnO_2$ core@shell nanowire arrays shown here, our smartly designed electrodes with the 3-D $ZnO@MnO_2$ core@shell nanoforest architecture are able to enhance the surface area and loading of electroactive MnO_2 on the same lateral footprint, while the 3-D ZnO nanotree backbone provides an ideal pathway for efficient charge transport. The main reasons behind the superior electrochemical performance of the nanoforest electrode possibly include: (i) more electroactive MnO_2 nanoparticles were coated onto the 3-D ZnO nanotrees with larger surface area than the nanowire arrays as the backbones with the same footprint; (ii) comparatively higher percentages of electroactive MnO_2 coating were deposited onto the ZnO branches than the ZnO trunk due to the smaller diameter of the former; and (iii) the extra loading of the coated electroactive MnO_2 nanoparticles on this novel 3-D ZnO nanoforest architecture over that of the nanowire array counterpart were also finely dispersed, directly grown on the current collector, and so still have fast charge transport paths.

Table 3 Discharging capacitance retention of the as-synthesized 3D ZnO@MnO_2 core@shell nanoforests and corresponding nanowire arrays at different current densities in the voltage range of -0.2 to 0.6 V (vs Ag/AgCl).

Electrode types	Current density [mA/cm^2]	Discharge time [s]	Capacitance [mF/cm^2]	Discharging capacitance retention [%]
ZnO@MnO_2 nanoforests	0.02	1251.970	31.299	100
	0.04	564.263	28.213	90.140
	0.06	368.280	27.621	88.248
	0.08	280.985	28.098	89.773
	0.10	226.985	28.373	90.651
	0.20	108.765	27.191	86.875
ZnO@MnO_2 nanowire arrays	0.02	252.172	6.304	100
	0.04	76.7017	3.835	60.833
	0.06	32.185	2.414	38.289
	0.08	22.5917	2.259	35.835
	0.10	13.8717	1.734	27.504
	0.20	6.68167	1.670	26.497

Moreover, the MnO_2 shell coating is amorphous, as confirmed by HRTEM and SAED (Figure 3.3). Amorphous MnO_2 was reported to be more desirable for supercapacitor applications owing to its high surface area and low mass density, compared with crystalline MnO_2.[77-78] The thin layer of amorphous MnO_2 enables fast and reversible faradaic reaction by a shortening ion diffusion path with large areal loading to achieve high specific capacitance while the 3-D ZnO nanotree backbone with high specific area provides highly conductive “highway” channels for effective electron transport. The novel design contributes to the superior capacitance and rate capability of our fabricated 3-D ZnO@MnO_2 core@shell nanoforests with reduced diffusion lengths of ions, highly accessible surface area and good electrical conductivity. Further studies are underway by integrating these novel 3-D ZnO@MnO_2 core@shell nanoforest electrodes into miniaturized LIBs and supercapacitors.

3.4 Conclusion

In summary, smartly designed 3-D ZnO@MnO_2 core@shell nanostructures have been successfully synthesized. These novel nanoarchitectures efficiently increase the accessible surface area of electroactive materials to the electrolyte, loading amount of electroactive materials per unit substrate area, and electrical conductivity of the hybrid electrode. The 3-D ZnO@MnO_2 core@shell nanoforest electrodes offer five times higher areal capacitances, advanced rate capability, and better charge-discharge stability, compared with their corresponding nanowire array counterpart. The present work indicates that our smartly designed 3-D nanoforest electrodes possess great application potentials for miniaturized energy storage devices.

CHAPTER IV

V2O5@PPY NANOFIBERS FOR ENERGY STORAGE

4.1 Introduction

Growing demands for rapidly powering portable electronics and electric vehicles has triggered substantial efforts on high-energy and high power-density energy storage devices.[17] Although possessing high energy density, lithium ion batteries (LIBs) are restricted in practical applications owing to short cycle life and low power delivery.[79] Therefore, pseudocapacitors attract extraordinary attentions and fill the gap with higher power density than LIBs and higher energy density than electrochemical double-layer capacitor, through rapid and reversible faradaic reactions.[80] Hybrid nanomaterials consisting of conductive polymer and transition metal oxides are considered as a smart approach to deliver higher specific energy.

To improve the performances of pseudocapacitors, numerous hybrid nanomaterials were designed by engineering electrically conductive polymers and transition metal oxides.

Among various transition metal oxides, vanadium oxide (V_2O_5) stands out as one of most promising ion insertion materials, due to its low-cost, abundance, layered structure, high energy density, and wide potential window arising from various vanadium oxidation states (V-II)[17, 79]. But its poor electronic conductivity, low structural stability, and high dissolution of vanadium ions into aqueous electrolyte are detrimental high-rate performances and rate stability applied in supercapacitors. Myriad efforts were donated to enhance the electron diffusion rate of V_2O_5 and further promote its capacitance. For example, Yan *et al.* coated V_2O_5 on SnO_2 nanowires to obtain high-power-density and high-energy density LIBs.[17] Chen *et al.* deposited V_2O_5 on mutiwall carbon nanotube (MWCNT) sponge backbone to serve as a high-performance cathode.[18] Chen *et al.* interpenetrated networks of carbon nanotubes (CNTs) and V_2O_5 nanowires for high energy and high power density supercapacitors.[15] Although these strategies can effectively improve electronic transport, they are still unable to prevent vanadium dissolution, which results in low cycling and rate stability. Recently, a core@shell structure of polypyrrole (PPy) grown on V_2O_5 nanoribbons exhibited high energy density, excellent cycling and good rate behavior as an promising anode material for supercapacitors. However, optimized ratio of PPy to V_2O_5 is not determined yet.

In this work, we integrated PPy and V_2O_5 nanofibers (NFs) into cablelike nanocomposites and ascertained the advisable ratio of PPy/V_2O_5, to maximize their specific capacitance and optimize rate stability. Forming PPy shell on the surface of V_2O_5 NFs will not only enhance electron migration and protect vanadium ions from dissolving into aqueous electrolyte, but also improve charge transport and allow deep penetration of electrolyte ions in electrode materials through reducing seamless entanglements between pristine V_2O_5 NFs. Meanwhile, the contributions from double layer capacitances and pseducapacitances were systematically analyzed with different amount PPy.

4.2 Experimental

4.2.1 Synthesis of V_2O_5 Nanofibers

Here, V_2O_5 NFs were prepared by a hydrothermal synthesis previously reported.[16] 0.30 g of ammonium metavanadate and 0.50 g of poly(ethylene oxide)-block-poly(propylene oxide)-block-poly(ethylene oxide) copolymer (P123) were dissolved in 30 mL of deioned water containing 1.5 mL of 2 M HCl. The mixture was stirred at room temperature for 24 h and then transferred into an autoclave and heated at 120 °C for 24 h. The resulting precipitate was rinsed with deioned water and acetone and then dried at 80 °C for 12 h.

4.2.2 Decoration of PPy on V_2O_5 Nanofibers

V_2O_5 NFs reinforced with PPy shell were fabricated by a surface-initiated polymerization method.[81] 0.10 g of pristine V_2O_5 NFs were initially mixed with the solution of *p*-toluenesulfonic acid (PTSA, $C_7H_8O_3S$) and (APS, $[(NH_4)_2S_2O_8]$) with a fixed ratio of 60 mmol: 36 mmol in 400 mL deionized water, following by 1 h vigorous stirring in an ice-water bath. The pyrrole (C_4H_5N) solution (74 mmol in 100 mL deionized water, molar ratio of APS: PTSA: pyrrole= 0.81: 0.49: 1) was added into the above V_2O_5 NFs suspended solution at 0 °C and then vigorously stirred for additional 1 h in an ice-water bath for further polymerization. The resultant solution turns from brown to greenish, indicating the polymerization of pyrrole. The product was precipitated naturally and washed with deionized water and methanol until the supernatant is transparent. V_2O_5 coated with varied amounts of PPy shells were achieved by tailoring the ratio of PPy/V_2O_5.

4.2.3 Characterization

The chemical composition, crystal structure, and morphology of the seeded substrate, as-prepared V_2O_5 nanofibers and V_2O_5@PPy were characterized through powder X-ray diffraction (XRD), Raman spectroscopy, scanning electron microscopy (SEM), electron backscatter diffraction(EBSD), transmission electron microscopy (TEM), high-resolution TEM (HRTEM), selected area electron diffraction (SAED) and energy dispersive X-ray spectroscopy (EDS). XRD analysis of the as-prepared ZnO samples was carried on with a Bruker AXS D8 QUEST diffractometer with Cu Kα radiation ($\lambda = 1.5406$ Å) between 25 ° and 70 °. Raman spectroscopy was conducted on a Bruker SENTERRA RAMAN microscope with a 785 nm laser as the excitation source. SEM and EBSD measurements were conducted on a Carl Zeiss Sigma VP Field-Emission scanning electron microscope at 2-5 kV. Transmission electron microscopy (TEM), high-resolution TEM (HRTEM) and selected-area electron diffraction (SAED) patterns were carried out on an Hitachi H-9500 microscope with an accelerating voltage of 300 kV. Specimens for the TEM studies were prepared by sonicating aqueous suspension containing as-prepared ZnO nanoforests, followed by depositing a drop of the suspension onto a 300 mesh Cu grid, coated with a lacey carbon film. To determine the mass ratio of PPy decorated on V_2O_5 NFs, thermogravimetric analysis (TGA) was performed from 25 °C to 600 °C at a heating rate of 10 °C/min on a Thermogravimetric Analyzer Q500 under air atmosphere.

4.2.4 Electrochemical Measurements

Electrochemical investigation of V_2O_5 and V_2O_5@PPy nanoribbons were conducted on a three electrode cell, which consists of the as-prepared V_2O_5 or V_2O_5@PPy electrodes as the working electrode, platinum wire as counter electrode and Ag/AgCl as the reference electrode. A syrup of the electrode material was prepared by blending 80 wt% of V_2O_5 or V_2O_5@PPy composites, 10 wt% of carbon black, and 10% PVDF with a few drops of DMF. This slurry mixture was coated on a carbon paper surface. It was followed by drying at 60 °C in vacuum oven overnight to obtain the working electrode. The electrochemical measurements were carried out in 1 M Na_2SO_4 aqueous electrolyte solution at room temperature.

To quantitatively evaluate the charge storage capacity, the specific capacitance C (in F/g) of the composite is accurately estimated based on this equation (1),

$$C = \frac{1000 \times \int_{E1}^{E2} i(E)dE}{2 \times (E2 - E1) \times m \times v}$$

where *E1* and *E2* are the cutoff potentials in cyclic voltammetry (in V), *i*(*E*) is the instantaneous current (A), $\int_{E1}^{E2} i(E)dE$ is the total voltammetric charge obtained by integration of positive and negative sweep in cyclic voltammograms. (*E2-E1*) is the potential window width. m is the mass of individual sample (in g), which is the mass difference of the working electrode before and after active deposition. *v* is the scan rate (in mV/s).[82]

On the other angel, the specific capacitance determined by charge-discharge curves can be calculated by the following equation (2),

$$C = \frac{i \times \Delta t}{m \times \Delta v}$$

Where i is the discharge current (in A), m is the mass of the electrode active material (in g), Δt is the discharging time (in s), and ΔV is the discharge potential (in V). The specific capacitance values reported for all samples have been calculated using the active mass of V_2O_5@PPy on the working electrodes.[83]

4.3 Results and Discussions

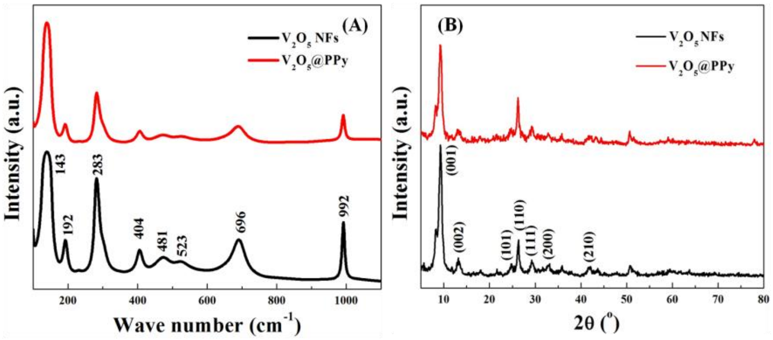

Figure 4.1 (A) Raman spectra and (B) XRD patterns of V_2O_5 NFs and V_2O_5@PPy.

Figure 4.1(A) shows the Raman Spectrum of V_2O_5 NFs and V_2O_5@PPy, in which the peaks locating at 143, 196, 283, 302, 404, 481, 523, 696 and 992 cm^{-1} can be assigned to the characteristic vibration modes of orthorhombic V_2O_5. Among them, the strongest peak at 143 cm^{-1} is attributed to the skeleton bent vibration, while the narrow peak at 992 cm^{-1} corresponds to the stretching vibration of vanadium atoms connected to oxygen atoms through double bonds, which is also a proof of the layered structure of V_2O_5. X-ray diffraction (XRD) patterns in Figure 4.1(B) display the characteristic peaks for V_2O_5 at $2\theta = 9.2°$, 13.1°, 24.2°, 25.4°, 28.8°, 32.0° and 41.1°, which are assigned to (001), (002), (101), (110), (111), (200), (210) and (020) lattice planes respectively.

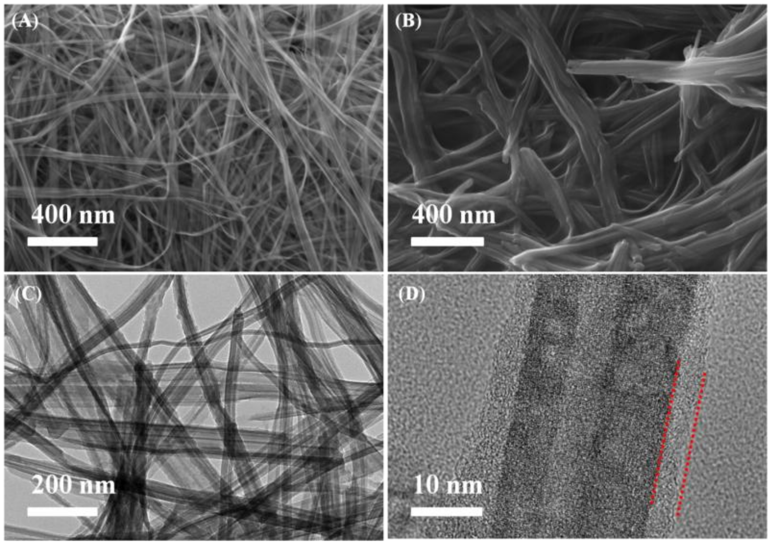

Figure 4.2 (A) SEM image of as prepared V_2O_5 nanofibers; (B) SEM image of as-prepared V_2O_5@PPy; (C) & (D) TEM and HRTEM images of as-prepared V_2O_5@PPy.

The morphology of the as-prepared V_2O_5 NFs and V_2O_5@PPy composite was studied by scanning electron microscopy (SEM). Typical SEM image of Figure 4.2(A) reveals that as-prepared V_2O_5 NFs have high aspect ratio and average diameter of ~30 nm. In Fig. 2(B), the diameter of V_2O_5@PPy composite was coupled and many expanded holes were formed between V_2O_5@PPy NFs, which is beneficial for electrolyte ions to penetrate deeply into electrode materials and rate capability. From EBSD pattern in Fig. 2S(A), the backbones of V_2O_5@PPy composites were clearly seen and V_2O_5 NFs were wrapped by conductive polymer PPy into cablelike. In the TEM image of Fig. 2(C), V_2O_5@PPy maintained nanofiber morphology but with rather rough surface, hinting the PPy coatings. High-resolution electron microscopy (HRTEM) image in Figure 4.2(D) confirmed the core@shell structure of the composite and the formation of PPy shell uniformly decorated on V_2O_5 surface. Thermogravimetry analysis (TGA) was applied to quantify the amount of PPy coating in the composite, shown in Figure 4.3.

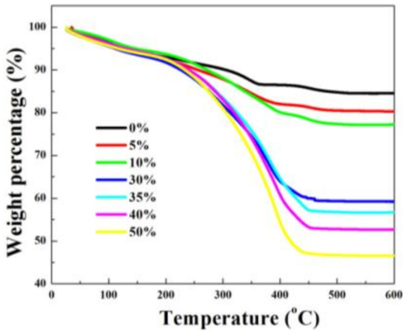

Figure 4.3 TGA curves of V_2O_5 with different ratios of PPy coatings

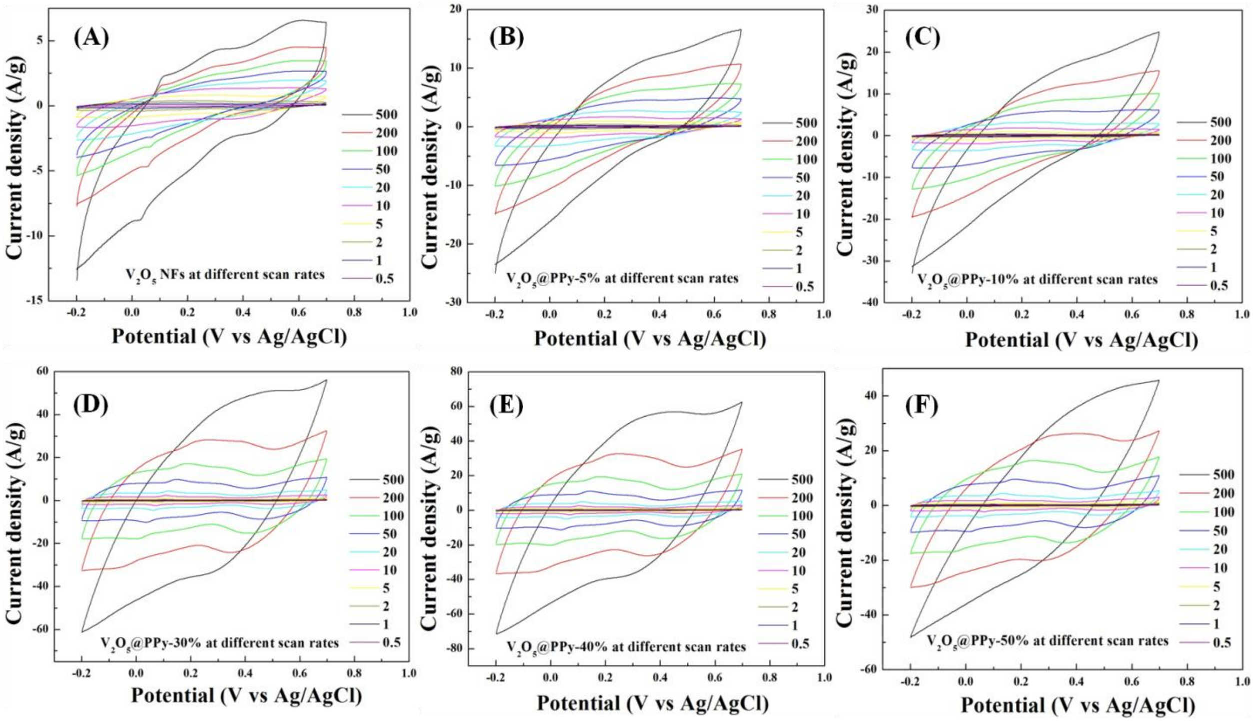

Figure 4.4 Cyclic Voltammetry curves of V_2O_5 coated with different mass ratios of PPy/V_2O_5 at scan rates of 0.5~500 mV/s: (A) V_2O_5@PPy-0%, (B) V_2O_5@PPy-5%, (C) V_2O_5@PPy-10%, (D) V_2O_5@PPy-30%, (E) V_2O_5@PPy-40%, (F) EDS pattern of as-prepared V2O5@PPy-50%.

All CV curves of each V_2O_5@PPy composite electrode were displayed with different PPy/V_2O_5 ratios and scan rates in Figure 4.4. At high scan rate of 500 mV/s, pristine V_2O_5 still displayed 6 small redox peaks in Figure 4.4(A) but V_2O_5@PPy-50% barely exhibited any redox peaks. It suggests that even at 500 mV/s electron-exchange reactions still occurred on V_2O_5 electrode.

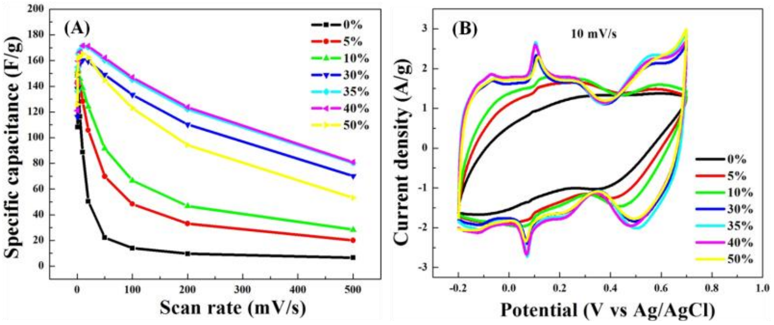

Figure 4.5 (A) Rate capability of V_2O_5@PPy composites with different ratios of PPy/V_2O_5 at scan rates of 0.5~500 mV/s; (B) cyclic voltammetry (CV) curves of corresponding V_2O_5@PPy composites at scan rate of 10 mV/s.

To investigate the electrochemical behavior, cyclic voltammogram (CV), charge-discharge (CD) measurements, and impedance (EIS) spectroscopy were conducted for V_2O_5@PPy composites with different ratios of PPy/V_2O_5. Fig. 3(A) presents the rate capability of V_2O_5@PPy composites at various scan rates of 0.5~500 mV/s. All the specific capacitances were calculated according to equation (1) and listed in Table 1. After comparing, an interesting phenomenon was noticed that, for the composites with distinct PPy/V_2O_5 ratios, the maximum specific capacitance appeared at various scan rates. For as-prepared V_2O_5 NFs, the highest capacitance of 142.9712 F/g was achieved at scan rate of 1 mV/s. When PPy/V_2O_5 ratios were 5% and 10%, their associated top capacitances of 151.2855 F/g and 152.2618 F/g were obtained at 2 mV/s. After the ratio reached 30% and more, their maximum capacitances were 160.3502, 171.4228, 171.6421, and 165.0741 F/g, respectively. The capacitance retention of each composite was revealed in Fig. 4S. Besides, after PPy/V_2O_5 ratio exceeded 40%, specific capacitances descended at each scan rate, which may be the result of PPy overcoating. Fig. 3(B) shows the CV curves of the V_2O_5@PPy electrodes in the anodic potential range of -0.2 to 0.7 V (vs Ag/AgCl). At a scan rate of 10 mV/s, the V_2O_5@PPy-40% electrode exhibits the most evident reversible current peaks, signifying the redox reaction of V_2O_5 related to its variable V valence states. When the PPy/V_2O_5 ratio reduced to 10%, the redox peaks for V_2O_5@PPy composites obviously shrank. Because low amount of PPy limited electron transportation as well as pseducapacitance contribution. V_2O_5@PPy exhibites a much better capacitance retention than V_2O_5 in Fig. 4S(A), which is attributed to the improved electronic conductivity of the composite derived from PPy shell.

Table 4 Specific capacitance of V_2O_5@PPy-*x* ratio at different scan rates.

Scan rate (mV/s)	0 (F/g)	5% (F/g)	10% (F/g)	30% (F/g)	35% (F/g)	40% (F/g)	50% (F/g)
500	6.651467	20.07276	28.35282	70.19672	80.28598	80.84007	53.30999
200	9.745031	33.1203	46.89728	110.195	122.0097	123.7328	94.36359
100	14.02194	48.3504	66.64066	133.4146	145.0128	146.9243	123.0453
50	22.21403	69.81132	91.6574	149.109	160.0734	162.1032	144.6457
20	50.49617	105.8127	124.1041	159.4011	170.2438	171.2742	162.361
10	88.78833	128.3559	138.6838	160.3502	171.4228	171.6421	165.0741
5	116.541	141.065	145.771	157.5901	167.9205	166.5373	163.2465
2	138.5187	151.2855	152.2618	153.9431	165.4074	159.5881	161.6439
1	142.9712	148.6658	151.866	137.9348	154.6931	142.8588	149.0074
0.5	108.1365	142.5721	148.3753	116.1072	135.9792	121.1724	125.895

The electrochemical Na^+ insertion/extraction process occuring at V_2O_5 electrodes can be expressed as,[83]

$$V_2O_5 + x\,Na^+ + x\,e^- \leftrightarrow Na_xV_2O_5$$

Conductive polymer shells significantly influenced electron and charge transportation during redox reaction. But few works were reported to investigated the mechanism of V_2O_5@PPy in aqueous electrolyte. Here, two kinds of capacitive contributions-double-layer capacitance and pseudocapacitance contributions-were respectively simulated according to all the CV curves in Fig. 3S. The area under curves represents the total stored charge originating from faradaic and non-faradaic processes. It can be explained by the power law $i = av^b$, where v is the scan rate, and both a and b are adjustable parameters. The parameter b is determined by the slope of the linear plot of log i versus log v. In general, slope $b = 1$ for surface redox reactions involving non-diffusion-controlled process, thus $i = av$. While for the ideal diffusion-controlled faradaic process. the slope b = 1/2 and satisfies Cottrell's equation: $i = av^{1/2}$.

Slope b is obtained by plotting log i versus log v as a function of voltage, V. It is noteworthy that the slope is ~0.5 at peak potentials indicating the dominance of the diffusion-limited process to overall charge storage, whereas the slope value is ~1 at other potentials indicating contribution of redox pseudocapacitance to charge storage, with "pseudo" referring to a faradaic reaction that is not diffusion-controlled. Therefore, the current response "i" at a given potential V, is the sum of two contributions arising from the redox pseudocapacitance and intercalation capacity as below.[84]

$$I = p_1 v + p_2 v^{1/2}$$

where $p_1 v$ and $p_2 v^{1/2}$ correspond to the current contributions from double layer capacitance and redox pseudocapacitance, respectively. Thus, by determining p_1 and p_2, it is possible to determine the current response due to electrostatic absorption and redox reaction at a specific potential. After simulation, the capacitance contributions were listed in Table 4. p_1 is determined by the product of the total surface area of electrodes, and p_2 is determined by the amount of pseudocapacitive storage (capacitance) per electrode surface area.

With PPy/V_2O_5 ratio varying from 30% to 50%, double layer capacitance firstly raised to 0.12302 at 40% and then reduced at 50%, which is determined by surface area. It suggests that overprotection of PPy shell restricted the surface area and access of electrolyte ions to electroactive materials. But pseudocapacitance contribution keep increasing with ascending PPy/V_2O_5 ratio, which is the result of good electron migration PPy shell providing.

Table 5 Capacitance contributions for each V_2O_5@PPy composite.

	30%	35%	40%	50%
p_1(double layer)	0.10229	0.12168	0.12302	0.08908
p_2(pseudo)	0.58572	0.60238	0.60509	0.6369
$p_1 + p_2$(total)	0.68801	0.72406	0.72811	0.72598

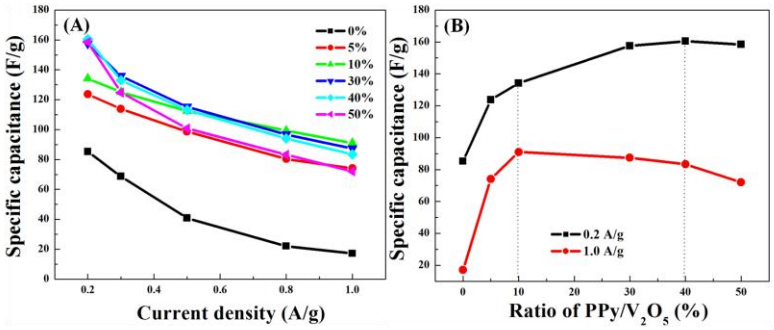

Figure 4.6 (A) Rate capability of V_2O_5@PPy composites arising from CD measurements at different current densities; (B) Rate capability of V_2O_5@PPy composites with different ratios of PPy/V_2O_5 at 0.2 A/g and 1.0 A/g, respectively.

Polymeric coating effect of PPy provided better electron migration pathway and also easier access of electrolyte ions to electroactive materials by weakening the entanglements between V_2O_5 NFs and increasing internal space between nanofibers. But overcoating of PPy is detrimental to the attachment between electrode materials and current collectors.

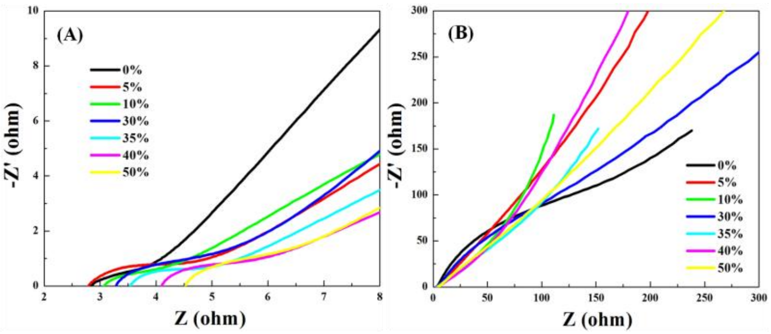

Figure 4.7 Nyquist plots for V_2O_5@PPy composites with different mass ratios of PPy/V_2O_5: 0%, 5%, 10% 30%, 35%, 40%, 50%.

Electrochemical impedance spectroscopy provides an effective method to analyze electrical conductivity and ion transfer of the related electrodes. Figure 4.7 exhibits Nyquist impedance spectra for V_2O_5@PPy composites in the frequency range of 0.01~ 5×10^5 Hz. Nyquist plot is a plot of the imaginary component (Z'') of the impedance against the vertical component (Z'). The lower left portion of the curve corresponds to the higher frequencies. According to the order of reducing frequency, the EIS spectra consists of three main regions. First, the intercept on the real axis in the high frequency range provides the equivalent series resistance, denoted as R_S, which represents the inherent resistance of electroactive material, ohmic resistance of the electrolyte, and contact resistance at the interface between electrolyte and electrode. Second, the charge transfer resistance ((R_{ct}) is determined by the diameter of semicircle in the high frequency range, revealing the diffusion of electrons. Third, Warburg resistance describes the diffusion of redox species in the electrolyte, which can be calculated by the slope of the EIS curve in low frequency range. The determined R_S values for V_2O_5@PPy composites with distinct PPy/V_2O_5 mass ratios of 0%, 5%, 10%, 30%, 40% and 50% are 2.85, 2.79, 3.07, 3.28, 3.54, 4.09, and 4.53 Ω , respectively. Compared with virgin V_2O_5 NFs, the slightly decreased R_S value for V_2O_5@PPy-5% was caused by enhanced electrical conductivity of electrode material after coating low amount of PPy on the surface of V_2O_5 NFs. However, the R_S values were gradually raised, with increasing mass ratios of PPy shell from 10% to 50%. It was the result of lowering adherence and loosing contact between electroactive materials and current collectors when PPy shells became thicker. This phenomenon was also observed in Figure 4.7. Moreover, the Nyquist plot for V_2O_5 NFs with the minimum slope (in Figure 4.7(B)) is derived from its inherently poor electron migration and poor ion diffusion in the structure of electrode due to tightly tangled V_2O_5 NFs blocking deep penetration of electrolyte ions. Thus, V_2O_5@PPy nanocomposite with a proper ratio of PPy/V_2O_5 is able to provide an ideal pathway for electrolyte ion and electron transport without kinetics limitations.

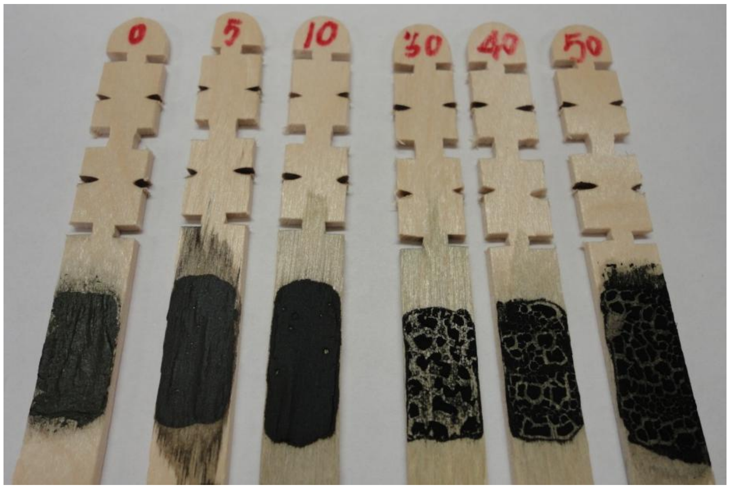

Figure 4.8 Digital pictures of V_2O_5@PPy composites with different mass ratios of PPy/V_2O_5: 0%, 5%, 10% 30%, 35%, 40%, 50%.

In Figure 4.8, it was clearly seen that electrode materials had trend to fall off the substrate and break into pieces, after the mass ratio of PPy/V_2O_5 raised 30%. Because coating conductive polymer PPy on the surface of V_2O_5 NFs reduced the interfacial contact between cablelike V_2O_5@PPy nanofibers and also blocked the adherence between electroactive materials and current collectors.

4.4 Conclusion

In summary, V_2O_5@PPy hybrid electrode was successfully fabricated via a two-step method. Benefiting from improved electron transfer, polymeric coating effect of PPy, and expanded internal space in electroactive materials, V_2O_5@PPy exhibited higher specific capacitance, better rate stability and lower inner resistance, and promising potentials to advance energy density of supercapacitors. The optimal ratio of PPy/V_2O_5 was determined at 40% and different capacitance contributions were also systematically investigated. Overcoating of PPy weakened the adherence between electroactive materials and current collector and restrained the total performances of electrodes. This work lays the foundation for outperformed hybrid electrode materials consisting of conductive polymer and transition metal oxide which applied in aqueous supercapacitors.

REFERENCES

1. F. E. Osterloh, and B. A. Parkinson. Recent developments in solar water-splitting photocatalysis, *Mrs Bull.*, 36, 17-22 (2011).
2. F. E. Osterloh. Inorganic nanostructures for photoelectrochemical and photocatalytic water splitting, *Chemical Society Reviews*, 42, 2294-2320 (2013).
3. T. S. Arthur, D. J. Bates, N. Cirigliano, D. C. Johnson, P. Malati, J. M. Mosby, E. Perre, M. T. Rawls, A. L. Prieto, and B. Dunn. Three-dimensional electrodes and battery architectures, *Mrs Bull,* 36, 523-531 (2011).
4. J. Jiang, Y. Y. Li, J. P. Liu, X. T. Huang, C. Z. Yuan, and X. W. Lou. Recent advances in metal oxide-based electrode architecture design for electrochemical energy storage, *Adv. Mater.*, 24, 5166-5180 (2012).
5. J. B. Goodenough, and K. S. Park. The Li-ion rechargeable battery: a perspective, *J. Am. Chem. Soc.*, 135, 1167-1176 (2013).
6. P. Simon, and Y. Gogotsi. Materials for electrochemical capacitors, *Nat. Mater.*, 7, 845-854 (2008).
7. G. H. Yu, L. B. Hu, M. Vosgueritchian, H. L. Wang, X. Xie, J. R. McDonough, X. Cui, Y. Cui, and Z. N. Bao Solution-processed graphene/MnO_2 nanostructured textiles for high-performance electrochemical capacitors, *Nano Lett.*, 11, 2905-2911 (2011).
8. A. L. M. Reddy, S. R. Gowda, M. M. Shaijumon, and P. M. Ajayan. Hybrid nanostructures for energy storage applications, *Adv. Mater.*, 24, 5045-5064 (2012).
9. J. T. Zhang, and X. S. Zhao. On the configuration of supercapacitors for maximizing Electrochemical Performance, *Chemsuschem*, 5, 818-841 (2012).
10. X. Chen, K. N. Sun, E. S. Zhang, and N. Q. Zhang. 3D porous micro/nanostructured interconnected metal/metal oxide electrodes for high-rate lithium storage, *RSC Adv.*, 3, 432-437 (2013).

11. S. H. Ko, D. Lee, H. W. Kang, K. H. Nam, J. Y. Yeo, S. J. Hong, C. P. Grigoropoulos, and H. J. Sung. Nanoforest of hydrothermally grown hierarchical ZnO nanowires for a high efficiency dye-sensitized solar cell, *Nano Lett.,* 11, 666-671 (2011).

12. X. Sun, Q. Li, Y. Lu, and Y. Mao. Three-dimensional ZnO@MnO_2 core@shell nanostructures for electrochemical energy storage, *Chem. Commun.,* 49, 4456-8 (2013).

13. J. P. Liu, J. Jiang, C. W. Cheng, H. X. Li, J. X. Zhang, H. Gong, and H. J. Fan. Co_3O_4 Nanowire@MnO_2 Ultrathin Nanosheet Core/Shell Arrays: A New Class of High-Performance Pseudocapacitive Materials, *Adv. Mater.,* **23**, 2076-2081 (2011).

14. X. H. Xia, J. P. Tu, Y. Q. Zhang, X. L. Wang, C. D. Gu, X. B. Zhao, and H. J. Fan. High-quality metal oxide core/shell nanowire arrays on conductive substrates for electrochemical energy storage, *ACS Nano,* 6, 5531-5538 (2012).

15. Z. Chen, V. Augustyn, J. Wen, Y. W. Zhang, M. Q. Shen, B. Dunn, and Y. F. Lu. High-performance supercapacitors based on intertwined CNT/V_2O_5 nanowire nanocomposites, *Adv. Mater.*, 23, 791-795 (2011).

16. C. R. Xiong, A. E. Aliev, B. Gnade, and K. J. Balkus. Fabrication of silver vanadium oxide and V_2O_5 nanowires for electrochromics, *ACS Nano,* 2, 293-301 (2008).

17. J. A. Yan, A. Sumboja, E. Khoo, and P. S. Lee. V_2O_5 loaded on SnO_2 nanowires for high-rate Li ion batteries, *Adv. Mater.*, 23, 746-750 (2011).

18. X. Y. Chen, H. L. Zhu, Y. C. Chen, Y. Y. Shang, A. Y. Cao, L. B. Hu, and G. W. Rubloff. MWCNT/V_2O_5 core/shell sponge for high areal capacity and power density Li-ion cathodes, *ACS Nano*, 6, 7948-7955 (2012).

19. M. Moniruzzaman, S. Sahoo, D. Ghosh, C. K. Das, and R. Singh. Preparation and characterization of polypyrrole/modified multiwalled carbon nanotube nanocomposites polymerized in situ in the presence of barium titanate, *J. Appl. Polym. Sci.,* 128, 698-705 (2013).

20. J. Joo, B. Y. Chow, M. Prakash, E. S. Boyden, and J. M. Jacobson. Face-selective electrostatic control of hydrothermal zinc oxide nanowire synthesis, *Nat. Mater.,* 10, 596-601 (2011).

21. M. Zhou, H. B. Wu, J. Bao, L. Liang, X. W. Lou, and Y. Xie. Ordered macroporous $BiVO_4$ architectures with controllable dual porosity for efficient solar water splitting, *Angew. Chem. Int. Ed. Engl.,* 52, 8579-83 (2013).

22. Z. Q. Sun, J. H. Kim, Y. Zhao, F. Bijarbooneh, V. Malgras, Y. Lee, Y. M. Kang, and S. X. Dou. Rational design of 3D dendritic TiO_2 nanostructures with favorable architectures, *J. Am. Chem. Soc.*, 133, 19314-19317 (2011).

23. T. L. Sounart, J. Liu, J. A. Voigt, M. Huo, E. D. Spoerke, and B. McKenzie. Secondary nucleation and growth of ZnO, *J. Am. Chem. Soc.*, 129, 15786-15793 (2007).

24. S. C. Warren, K. Voitchovsky, H. Dotan, C. M. Leroy, M. Cornuz, F. Stellacci, C. Hebert, A. Rothschild, and M. Gratzel. Identifying champion nanostructures for solar water-splitting, *Nat. Mater.*, 12, 842-849 (2013).

25. T. R. Zhang, W. J. Dong, M. Keeter-Brewer, S. Konar, R. N. Njabon, and Z. R. Tian. Site-specific nucleation and growth kinetics in hierarchical nanosyntheses of branched ZnO crystallites, *J. Am. Chem. Soc.*, 128, 10960-10968 (2006).

26. Z. L. Wang. From nanogenerators to piezotronics-A decade-long study of ZnO nanostructures, *Mrs Bull.*, 37, 814-827 (2012).

27. R. Kozhummal, Y. Yang, F. Guder, A. Hartel, X. L. Lu, U. M. Kucukbayrak, A. Mateo-Alonso, M. Elwenspoek, and M. Zacharias. Homoepitaxial branching: an unusual polymorph of zinc oxide derived from seeded solution growth, *ACS Nano*, 6, 7133-7141 (2012).

28. S. Xu, and Z. L. Wang. One-dimensional ZnO nanostructures: solution growth and functional properties, *Nano Res.*, 4, 1013-1098 (2011).

29. Z. L. Wang, R. Guo, L. X. Ding, Y. X. Tong, and G. R. Li. Controllable template-assisted electrodeposition of single- and multi-walled nanotube arrays for electrochemical energy storage, *Sci. Rep.*, 3, 1204 (2013).

30. Q. Kuang, Z. Y. Jiang, Z. X. Xie, S. C. Lin, Z. W. Lin, S. Y. Xie, R. B. Huang, and L. S. Zheng. Tailoring the optical property by a three-dimensional epitaxial heterostructure: A case of ZnO/SnO_2, *J. Am. Chem. Soc.*, 127, 11777-11784 (2005).

31. S. Cho, S. H. Jung, and K. H. Lee. Morphology-controlled growth of ZnO nanostructures using microwave irradiation: from basic to complex structures, *J. Phys. Chem. C,* 112, 12769-12776 (2008).

32. J. Shi, H. Hong, Y. Ding, Y. A. Yang, F. Wang, W. B. Cai, and X. D. Wang. Evolution of zinc oxide nanostructures through kinetics control, *J. Mater. Chem.*, 21, 9000-9008 (2011).

33. W. W. Lee, J. Yi, S. B. Kim, Y. H. Kim, H. G. Park, and W. I. Park. Morphology-controlled three-dimensional nanoarchitectures produced by exploiting vertical and in-plane

crystallographic orientations in hydrothermal ZnO crystals, *Cryst. Growth Des.*, 11, 4927-4932 (2011).

34. H. S. Song, W. J. Zhang, C. Cheng, Y. B. Tang, L. B. Luo, X. Chen, C. Y. Luan, X. M. Meng, J. A. Zapien, N. Wang, C. S. Lee, I. Bello, and S. T. Lee. Controllable fabrication of three-dimensional radial ZnO nanowire/silicon microrod hybrid architectures, *Cryst. Growth Des.*, 11, 147-153 (2011).

35. W. D. Shi, S. Y. Song, and H. J. Zhang. Hydrothermal synthetic strategies of inorganic semiconducting nanostructures, *Chemical Society Reviews*, 42, 5714-5743 (2013).

36. Z. R. R. Tian, J. A. Voigt, J. Liu, B. McKenzie, M. J. McDermott, M. A. Rodriguez, H. Konishi, and H. F. Xu. Complex and oriented ZnO nanostructures, *Nat. Mater.*, 2, 821-826 (2003).

37. K. S. Kim, H. Jeong, M. S. Jeong, and G. Y. Jung. Polymer-templated hydrothermal growth of vertically aligned single-crystal ZnO nanorods and morphological transformations using structural polarity, *Adv. Funct. Mater.*, 20, 3055-3063 (2010).

38. A. Soudi, P. Dhakal, and Y. Gu. Diameter dependence of the minority carrier diffusion length in individual ZnO nanowires, *Appl. Phys. Lett.*, 96, 253115 (2010).

39. K. F. Liu, W. B. Wu, B. L. Chen, X. D. Chen, and N. N. Zhang. Continuous growth and improved PL property of ZnO nanoarrays with assistance of polyethylenimine, *Nanoscale*, 5, 5986-5993 (2013).

40. T. Shinagawa, S. Watase, and M. Izaki. Size-controllable growth of vertical ZnO nanorod arrays by a Pd-catalyzed chemical solution process, *Cryst. Growth Des.*, 11, 5533-5539 (2011).

41. M. Law, L. E. Greene, J. C. Johnson, R. Saykally, and P. D. Yang. Nanowire dye-sensitized solar cells, *Nat. Mater.*, 4, 455-459 (2005).

42. L. Y. Chen, Y. T. Yin, C. H. Chen, and J. W. Chiou. Influence of polyethyleneimine and ammonium on the growth of ZnO nanowires by hydrothermal method, *J. Phys. Chem. C*, 115, 20913-20919 (2011).

43. M. J. Bierman, and S. Jin. Potential applications of hierarchical branching nanowires in solar energy conversion, *Energ. Environ. Sci.*, 2, 1050-1059 (2009).

44. H. H. Li, Y. Y. Fu, H. X. Liu, M. Y. Zhu, Z. Peng, J. Yang, J. Li, X. Y. Huang, Y. Jiang, Q. Q. Liu, X. J. Shi, H. Wu, Y. H. Yang, and Q. Liu. Defect-controlled ZnO nanorod arrays for enhanced photoelectrochemical performance, *Inorg. Chem. Commun.*, 30, 182-186 (2013).

45. Y. C. Qiu, K. Y. Yan, H. Deng, and S. H. Yang. Secondary branching and nitrogen doping of ZnO nanotetrapods: building a highly active network for photoelectrochemical water splitting, *Nano Lett.,* 12, 407-413 (2012).

46. K. M. McPeak, T. P. Le, N. G. Britton, Z. S. Nickolov, Y. A. Elabd, and J. B. Baxter. Chemical bath deposition of ZnO nanowires at near-neutral pH conditions without Hexamethylenetetramine (HMTA): understanding the role of HMTA in ZnO nanowire growth, *Langmuir,* 27, 3672-3677 (2011).

47. O. Lupan, T. Pauporte, L. Chow, B. Viana, F. Pelle, L. K. Ono, B. R. Cuenya, and H. Heinrich. Effects of annealing on properties of ZnO thin films prepared by electrochemical deposition in chloride medium, *Appl. Surf. Sci.,* 256, 1895-1907 (2010).

48. H. T. Nguyen, F. Yao, M. R. Zamfir, C. Biswas, K. P. So, Y. H. Lee, S. M. Kim, S. N. Cha, J. M. Kim, and D. Pribat. Highly interconnected Si nanowires for improved stability Li-ion battery anodes, *Adv. Energy Mater.,* 1, 1154-1161 (2011).

49. I. Herman, J. Yeo, S. Hong, D. Lee, K. H. Nam, J. H. Choi, W. H. Hong, D. Lee, C. P. Grigoropoulos, and S. H. Ko. Hierarchical weeping willow nano-tree growth and effect of branching on dye-sensitized solar cell efficiency, *Nanotechnology,* 23, 194005-194009 (2012).

50. A. I. Hochbaum, and P. D. Yang. Semiconductor nanowires for energy conversion, *Chem. Rev.,* 110, 527-546 (2010).

51. A. Wolcott, W. A. Smith, T. R. Kuykendall, Y. P. Zhao, and J. Z. Zhang. Photoelectrochemical study of nanostructured ZnO thin films for hydrogen generation from water splitting, *Adv. Funct. Mater.,* 19, 1849-1856 (2009).

52. K. S. Ahn, Y. Yan, S. Shet, K. Jones, T. Deutsch, J. Turner, and M. Al-Jassim. ZnO nanocoral structures for photoelectrochemical cells, *Appl. Phys. Lett.,* 93, 163117 (2008).

53. Y. F. Wei, L. Ke, J. H. Kong, H. Liu, Z. H. Jiao, X. H. Lu, H. J. Du, and X. W. Sun. Enhanced photoelectrochemical water-splitting effect with a bent ZnO nanorod photoanode decorated with Ag nanoparticles, *Nanotechnology,* 23, 235401-235408 (2012).

54. X. Y. Yang, A. Wolcott, G. M. Wang, A. Sobo, R. C. Fitzmorris, F. Qian, J. Z. Zhang, and Y. Li. Nitrogen-doped ZnO nanowire arrays for photoelectrochemical water splitting, *Nano Lett.,* 9, 2331-2336 (2009).

55. C. Liu, X. B. Xu, A. J. E. Rettie, C. B. Mullins, and D. L. Fan. One-step waferscale synthesis of 3-D ZnO nanosuperstructures by designed catalysts for substantial improvement of solar water oxidation efficiency, *J. Mater. Chem. A*, 1, 8111-8117 (2013).

56. B. Klahr, S. Gimenez, F. Fabregat-Santiago, T. Hamann, and J. Bisquert. Water oxidation at Hematite photoelectrodes: the role of surface states, *J. Am. Chem. Soc.*, 134, 4294-4302 (2012).

57. A. Zaban, M. Greenshtein, and J. Bisquert. Determination of the electron lifetime in nanocrystalline dye solar cells by open-circuit voltage decay measurements, *ChemPhysChem*, 4, 859-864 (2003).

58. Y. J. Lin, Y. Xu, M. T. Mayer, Z. I. Simpson, G. McMahon, S. Zhou, and D. W. Wang. Growth of p-type Hematite by atomic layer deposition and its utilization for improved solar water splitting, *J. Am. Chem. Soc.*, 134, 5508-5511 (2012).

59. I. S. Cho, Z. B. Chen, A. J. Forman, D. R. Kim, P. M. Rao, T. F. Jaramillo, and X. L. Zheng. Branched TiO_2 nanorods for photoelectrochemical hydrogen production, *Nano Lett.*, 11, 4978-4984 (2011).

60. J. S. Yang, W. P. Liao, and J. J. Wu. Morphology and interfacial energetics controls for hierarchical anatase/rutile TiO_2 nanostructured array for efficient photoelectrochemical water splitting, *ACS Appl. Mater. Interfaces*, 5, 7425-31 (2013).

61. X. Lu, H. J. Zhou, G. J. Salamo, Z. R. Tian, and M. Xiao. Generation of exciton-polaritons in ZnO microcrystallines using second-harmonic generation, *New J. Phys.*, 14, 1-10 (2012).

62. H. G. Kim, P. H. Borse, J. S. Jang, C. W. Ahn, E. D. Jeong, and J. S. Lee. Engineered nanorod perovskite film photocatalysts to harvest visible light, *Adv. Mater.*, 23, 2088-2092 (2011).

63. H. M. Chen, C. K. Chen, R. S. Liu, L. Zhang, J. Zhang, and D. P. Wilkinson. Nano-architecture and material designs for water splitting photoelectrodes, *Chem. Soc. Rev.*, 41, 5654-71 (2012).

64. S. Cho, J. W. Jang, K. J. Kong, E. S. Kim, K. H. Lee, and J. S. Lee. Anion-doped mixed metal oxide nanostructures derived from layered double hydroxide as visible light photocatalysts, *Adv. Funct. Mater.*, 23, 2348-2356 (2013).

65. Z. F. Wang, P. Xiao, L. Qiao, X. Q. Meng, Y. H. Zhang, X. L. Li, and F. Yang Polypyrrole sensitized ZnO nanorod arrays for efficient photo-electrochemical splitting of water, *Physica B,* 419, 51-56 (2013).

66. M. Gratzel. Photoelectrochemical cells, *Nature*, 414, 338-44 (2001).

67. B. Liu, H. M. Chen, C. Liu, S. C. Andrews, C. Hahn, and P. Yang. Large-scale synthesis of transition-metal-doped TiO_2 nanowires with controllable overpotential, *J. Am. Chem. Soc.*, 135, 9995-9998 (2013).

68. Y. Y. Bu, Z. Y. Chen, W. B. Li, and J. Q. Yu. High-efficiency photoelectrochemical properties by a highly crystalline CdS-sensitized ZnO nanorod array, *ACS Appl. Mater. Inter.*, 5, 5097-5104 (2013).

69. Z. Y. Yin, Z. Wang, Y. P. Du, X. Y. Qi, Y. Z. Huang, C. Xue, and H. Zhang. Full solution-processed synthesis of all metal oxide-based tree-like heterostructures on fluorine-doped tin oxide for water splitting, *Adv. Mater.,* 24, 5374-5378 (2012).

70. H. Jiang, C. Z. Li, T. Sun, and J. Ma. High-performance supercapacitor material based on $Ni(OH)_2$ nanowire-MnO_2 nanoflakes core-shell nanostructures, *Chem. Commun.,* 48, 2606-2608 (2012).

71. S. Xin, Y. G. Guo, and L. J. Wan. Nanocarbon networks for advanced rechargeable lithium batteries, *Accounts Chem. Res.*, 45, 1759-1769 (2012).

72. L. Q. Mai, F. Yang, Y. L. Zhao, X. Xu, L. Xu, and Y. Z. Luo. Hierarchical $MnMoO_4/CoMoO_4$ heterostructured nanowires with enhanced supercapacitor performance, *Nat. Commun.,* 2, (2011).

73. H. G. Wei, X. R. Yan, S. J. Wu, Z. P. Luo, S. Y. Wei, and Z. H. Guo. Electropolymerized polyaniline stabilized tungsten oxide nanocomposite films: electrochromic behavior and electrochemical energy storage, *J. Phys. Chem. C,* 116, 25052-25064 (2012).

74. C. W. Cheng, and H. J. Fan. Branched nanowires: synthesis and energy applications, *Nano Today*, 7, 327-343 (2012).

75. H. Wu, M. Xu, Y. C. Wang, and G. F. Zheng. Branched Co_3O_4/Fe_2O_3 nanowires as high capacity lithium-ion battery anodes, *Nano Res.,* 6, 167-173 (2013).

76. R. B. Rakhi, W. Chen, D. Y. Cha, and H. N. Alshareef. Substrate dependent self-organization of mesoporous cobalt oxide nanowires with remarkable pseudocapacitance, *Nano Lett.,* 12, 2559-2567 (2012).

77. L. H. Bao, J. F. Zang, and X. D. Li. Flexible Zn_2SnO_4/MnO_2 core/shell nanocable-carbon microfiber hybrid composites for high-performance supercapacitor electrodes, *Nano Lett.*, 11, 1215-1220 (2011).

78. J. G. Wang, Y. Yang, Z. H. Huang, and F. Y. Kang. Rational synthesis of MnO_2/conducting polypyrrole@carbon nanofiber triaxial nano-cables for high-performance supercapacitors, *J. Mater. Chem.*, 22, 16943-16949 (2012).

79. Q. T. Qu, Y. S. Zhu, X. W. Gao, and Y. P. Wu. Core-shell structure of polypyrrole grown on V_2O_5 nanoribbon as high performance anode material for supercapacitors, *Adv. Energy Mater.*, 2, 950-955 (2012).

80. J. W. Long, D. Belanger, T. Brousse, W. Sugimoto, M. B. Sassin, and O. Crosnier. Asymmetric electrochemical capacitors-Stretching the limits of aqueous electrolytes, *MRS Bull.*, 36, 513-522 (2011).

81. J. H. Zhu, S. Y. Wei, L. Zhang, Y. B. Mao, J. Ryu, P. Mayinakuli, A. B. Karki, D. P. Young, and Z. H. Guo. Conductive polypyrrole/tungsten oxide metacomposites with negative permittivity, *J. Phys. Chem. C*, 114, 16335-16342 (2010).

82. W. Chen, Z. L. Fan, L. Gu, X. H. Bao, and C. L. Wang. Enhanced capacitance of manganese oxide via confinement inside carbon nanotubes, *Chem. Commun.*, 46, 3905-3907 (2010).

83. B. Saravanakumar, K. K. Purushothaman, and G. Muralidharan. Interconnected V_2O_5 nanoporous network for high-performance supercapacitors, *ACS Appl. Mater. Inter.*, **4**, 4484-4490 (2012).

84. K. Zhu, Q. Wang, J. H. Kim, A. A. Pesaran, and A. J. Frank. Pseudocapacitive lithium-ion storage in oriented anatase TiO_2 nanotube arrays, *J. Phys. Chem. C*, 116, 11895-11899 (2012).

BIOGRAPHICAL SKETCH

Xing Sun, was born in 1986 in Liaocheng City, China. She obtained her high school degree from Liaocheng NO. 1 Middle School in 2004. Then she was granted the bachelor of engineering degree in Materials Science and Engineering Department of the Nanjing University of Technology in 2008, where she had served as an undergraduate research assistant under the supervision of Professor Yinong Lv. She attempted to pursue overseas education in the US and then was accepted to the University of Texas-Pan American (UTPA) in 2011 in order for a master of science degree in Chemistry Department. There she started to work as a graduate research assistant under the supervision of Dr. Yuanbing Mao on the thesis topic, metal oxide nanostructures for energy conversion and storage. She finished her studies in May 2014.

Her permanent address is:
Xing Sun
Apt 205, Unit 7, NO. 26
Guanqian Street
Dongchangfu District
Liaocheng City
Shandong Province
P.R.China